Chapter 5

Functionalized fullerene-C_{60}-TiO_2 nanostructures composites for efficient VOC sensing

5.1 Introduction

Fullerene, the third allotrope of carbon having a cage like structure exists in different forms like -C_{60}, C_{70}, C_{20} [1]. C_{60} fullerene is composed of five to six sp^2 hybridized carbon rings developing a cut off icosahedron structure. This cage like structure of fullerene comprises of hexagons and pentagons with interchanging single and double bond [2],[3]. Fullerene-C_{60} molecules are highly active because of its curved structure providing high energy to its double bonds. Fullerene possesses both electrophilic and nucleophilic behaviour with a fondness towards electrons. Electron deficient nature of fullerene is due to the presence of unstable double bonds at the pentagon rings. Different fascinating electrochemical properties are possessed by C_{60} fullerene like strong enormous surface to volume ratio, stable structure, long living triplet state, plenty of conjugated π electrons and multiple redox states [4].

Individual fullerene and functionalized fullerene both are supportive in different domains of nanoscience. Functionalization of fullerene drives it potentially with more stability and enhanced hydrophilicity [5]. Functionalized fullerene has a high catalytic activity due to the attached functional groups or radicals that enhance its surface reactivity. Hydration or oxidation of fullerene give rise to the different functional groups attached on its surface which participate majorly while synthesizing fullerene-based nanocomposites or different hybrids [4]. Different methods have been proposed to synthesize aqueous solution of fullerene with the aim to produce a reasonable nanomaterial having a high electron transport property [6-8]. Also, some reports have been published depicting the advantages of functionalized fullerene with regard to the nanocomposite synthesis and further representing the outspread applications [9-11].

The biocompatible and non-toxic nature of fullerene with antioxidant properties, has made fullerene an alluring nanomaterial in the field of biosensors, clinical diagnosis and medicinal chemistry [12]. Many articles have been published reporting fullerene-C_{60} and its nanocomposites as a dominant candidate in biosensors and pharmaceutical applications. Sutradhar and Patnaik have reported non-enzymatic sensing characteristics for glucose detection by functionalized fullerene-C_{60} and Au nanocomposite. They have proposed a sensor

showing high response magnitude ($1.2\mu A$ $mM^{-1}cm^{-2}$) with prolonged stability and anti-interference property [1]. Long and co-workers have demonstrated ultrasensitive DNA detection by a photoelectrical biosensor based on methylene blue synthesized fullerene C_{60} [13]

Multiple properties of fullerene have prompted researchers to explore its properties in different fields but a very few experiments are carried out on fullerene or fullerene-nanocomposite based chemical sensors. Furuuchi and group synthesized melon shaped nano porous fullerene-C_{60} crystals using liquid-liquid interfacial precipitation method. They have shown the nanoporous structure supports easy diffusion and π-π interaction with sp^2 carbon enables excellent aromatic vapor sensing [14]. Rather and group have synthesized an electrochemical sensor by immobilizing C_{60} particles on glassy carbon electrode for trace detection of bisphenol [15]. Smazna and co-workers fabricated ZnO tetrapod enveloped with variable C_{60} flooding and investigated the nanocomposite for efficient detection of ethanol [16]. Keshtkar and group have prepared SnO_2-quantum dot and fullerene nanohybrid by hydrothermal method for selective detection of H_2S at 200 ˚C [17].

To attain a high surface to the available volume, modern synthesis methods have been applied by the researchers as compared to the accustomed techniques. Distinctive nanostructures having unique dimensions hold different properties. Zero-dimensional (0-D) nanomaterial is one of the most promising material with its unique nature. Excessive small size with large functioning edges per unit mass and the quantum confinement effect makes 0-D materials supreme among other nanomaterials [18]. One dimensional (1-D) nanostructures like wires, tubes, rods, belts etc. have highly crystalline, undeviating and stable structure [19],[20]. Highly porous 1-D nanotubes are significant as they can provide a strong base to the nanocrystals of fullerene in composite form. However, a porous nanostructure on which fullerene nanocrystals can be decorated homogeneously increases the amount of accessibility to surface interaction sites significantly [16]. Similarly, two zero-dimensional nanoforms - fullerene and TiO_2 nanoparticles can also be combined to form a nanohybrid.

This current chapter describes the fabrication of two different types C_{60}-TiO_2 nanostructure composites. C_{60}-TiO_2 nanotubes array composites were synthesized by hydrothermal method where five different samples were prepared by increasing the concentration of fullerene-C_{60} varying from 0 wt% to 0.05 wt% on electrochemically grown TiO_2 nanotubes. All the samples were examined through morphological, structural and optical characterizations. All the sensors were subjected to variety of VOCs where highest sensitivity was achieved towards

formaldehyde. C_{60} fullerene particles were also decorated with TiO_2 nanoparticles, the structure was looking like C_{60} encapsulated TiO_2 nanoparticles. TiO_2 nanoparticles were fully covered with C_{60}. The C_{60}- TiO_2 nanoparticles composite was synthesized via chemical route by using hydrated fullerene-C_{60} and sol-gel derived undoped p-type TiO_2 nanoparticles. The nanocomposite was characterized morphologically and structurally comparing with pure C_{60} clusters and pure TiO_2 nanoparticles as the reference materials.

5.2 C_{60} -TiO_2 nanotubes composites

5.2.1 Synthesis

1-D TiO_2 nanotubes have been synthesized using electrochemical anodization route that has been previously described in section 2.2.1 of chapter 2. High purity fullerene-C_{60} from Sigma Aldrich (99.9%) was used to prepare the aqueous solution of fullerene. Four different weight percent water soluble fullerene solutions were prepared by a two-step process. The detailed procedure to functionalize the fullerene nanoparticles has been explained in chapter 2.

Preparation of nanocomposite
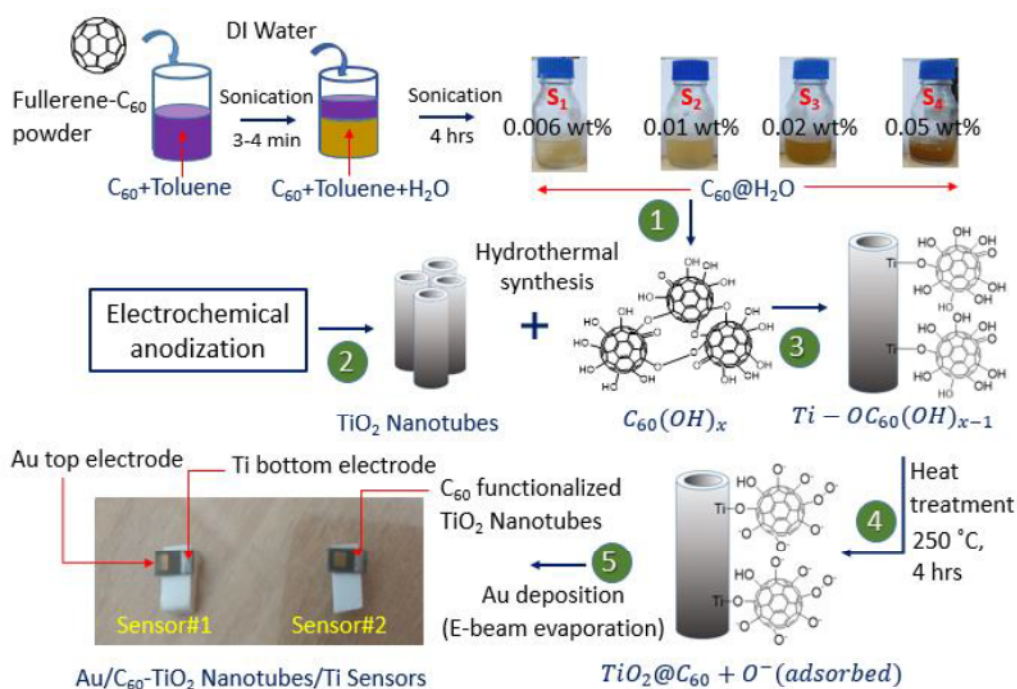
Fig. 5.1. Four major steps i.e. the synthesis of fullerene-C_{60} water colloidal system, anodic growth of the TiO_2 nanotubes array, hydrothermal synthesis of fullerene-C_{60}/TiO_2 nanotubes composites and fabrication of the metal-insulator-metal (MIM) structured sensors, are shown in the flow diagram.

The nanocomposite was prepared by hydrothermal method where four pure TiO_2 nanotube array samples were dipped in four different fullerene-C_{60} solutions with varied weight

percentage i.e. 0.006, 0.01, 0.02 and 0.05 wt%. All the samples were then kept inside a teflon lined stainless steel autoclave of 100 ml volume. The process was performed at 180 ℃ for 12 hours in hot air oven. All the synthesized C_{60}-TiO_2 composite samples (S_1-S_4) were cleaned with DI water and ethanol and then dried in air at 250 ℃ for four hours.

Formation of functionalized C_{60} with TiO_2

Both hydrated individual fullerene molecules $[C_{60}@(H_2O)_n]$ and spherical fullerene clusters of variable sizes $[\{C_{60}@(H_2O)_n\}_m]$ exist in the fullerene water colloidal system. Fullerene aqueous solution is composed of the spherical shells of linked water molecules around the C_{60} molecules which are formed by the transfer of electrons from oxygen atoms of water to the fullerene molecule via the formation weak donor acceptor bond in the C_{60}-H_2O complex [21]. Formation of fullerol from fullerene enhances the hydrophilicity and raises the different oxygen functionalization groups which in turn helps in formation of stable composite (Fig. 5.1) [5]. The negative charge on fullerene clusters is due to movement of electrons from oxygen atoms to fullerene molecules and the formation of H^+ ions (Eq.5.1) [21].

$$mC_{60}+:OH_2 \leftrightarrow [\{mC_{60}\} \leftarrow:OH]^- + H^+ \tag{5.1}$$

Considering the above discussions, hydrated fullerene $[C_{60}@(H_2O)_n]$ can be represented as $C_{60}@\{xOH^-.yH_2O\}^{x-}.xH^+$, where n is the total number of water molecules existing in both the ionized (x) and non-ionized (y) states and x+y=n [21]. However, depending on the concentrations of fullerene-C_{60} in the water colloidal system, $C_{60}@(H_2O)_n$ can form different clusters of different sizes. In the current study, four different concentrations (0.006, 0.01, 0.02 and 0.05 wt%) of fullerene-C_{60} were used to synthesize four different water colloidal systems as shown in Fig. 5.1.

C_{60} or functionalized C_{60} (i.e. hydrated fullerene or fullerol) clusters form covalent bonds with TiO_2 ($\equiv$Ti-OH) upon formation of nanocomposite. Synthesized nanocomposite is composed of hydroxyl groups interlinked to TiO_2 with many oxygen links as represented in Eq.5.2 and in Fig. 5.1 [22][23].

$$Ti-OH+OH-C_{60}(OH)_{x-1} \rightarrow \equiv Ti-OC_{60}(OH)_{x-1} + H_2O \tag{5.2}$$
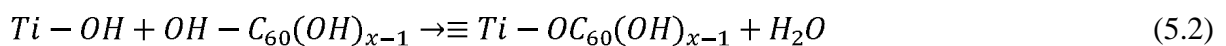
Aqueous colloidal solution of fullerene consisting of individual fullerene molecules and clusters provides high stabilization and activation on being decorated on TiO_2 nanotubes. Depending on the concentrations of the C_{60} in four different colloidal solutions, size of the C_{60} clusters were different in four composites of C_{60}-TiO_2 nanotubes.

So, the clustered and individual fullerene-C_{60}, functionalized with a large number of oxygen species, forming a composite with TiO_2 nanotubes were investigated for the VOC sensing in the current study.

5.2.2 Characterization

Morphological characterization
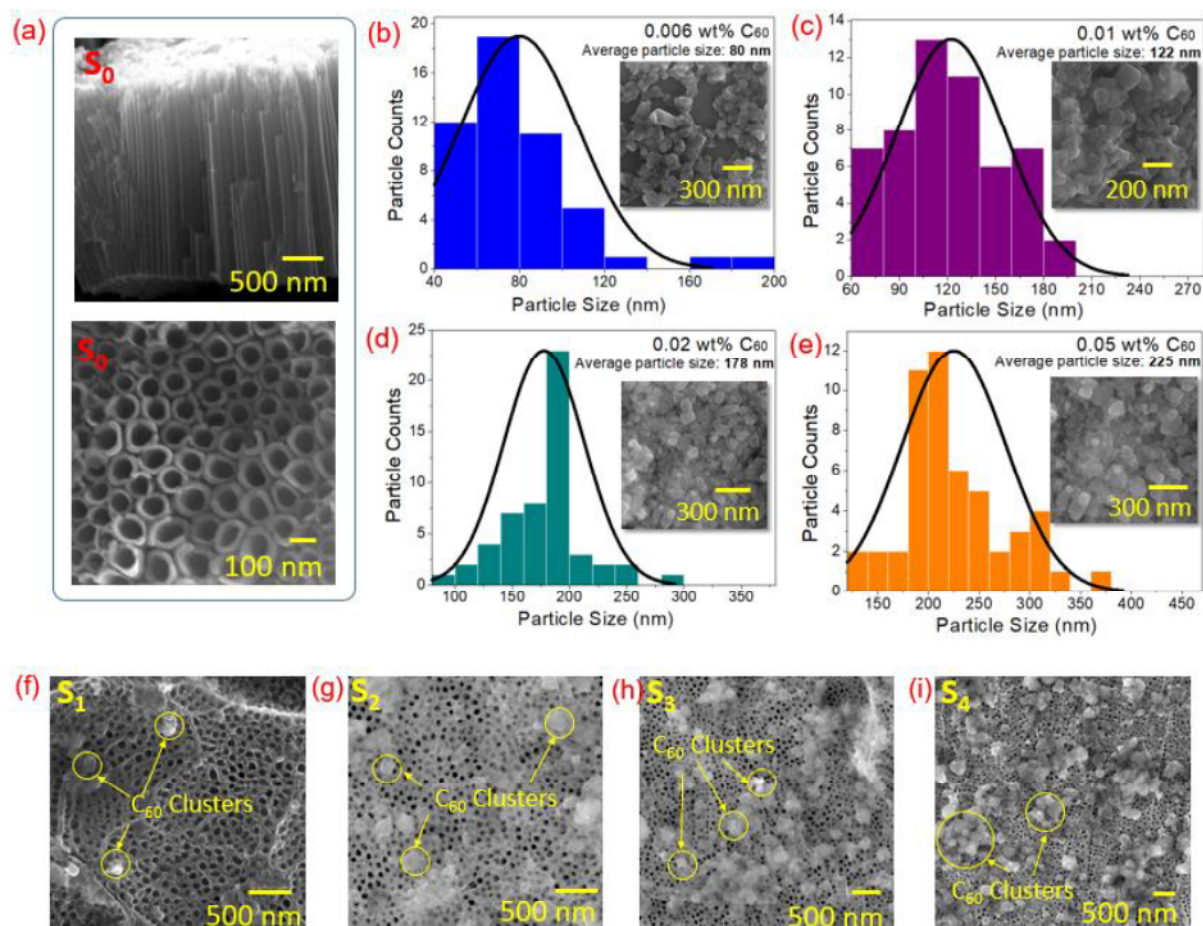
Fig. 5.2. (a) Scanning electron micrograph (SEM) of pure TiO_2 nanotubes array (i.e. S_0) indicating the side and top views. Analysis of cluster (particle) size of C_{60} having different concentrations i.e. C_{60} i.e. (b) 0.006 wt%, (c) 0.01 wt%, (d) 0.02 wt% and (e) 0.05 wt%. SEM images of C_{60}-TiO_2 composites with different concentrations of C_{60} i.e. (f) S_1 (0.006 wt% C_{60}), (g) S_2 (0.01 wt% C_{60}), (h) S_3 (0.02 wt% C_{60}) and (i) S_4 (0.05 wt% C_{60}).

The highly ordered morphology of the pure TiO_2 nanotubes array is shown in Fig. 5.2(a). Size distribution of spherical C_{60}-clusters for different concentrations C_{60} is shown in Fig. 5.2(b-e). Particle size distribution was carried out from the FESEM images (inset in Fig. 5.2(b-e)) of pure C_{60} clusters synthesized from the solution of different concentrations of C_{60} (i.e. 0.006 to 0.05 wt%). The size of the C_{60}-cluster was measured with ImageJ software and plotted in the form of particle counts as a function of particle size in nm in Fig. 5.2(b-e). The average cluster size was increased with increase of C_{60} concentration in the solution. The average cluster size

112

was measured as 80 nm, 122 nm, 178 nm, and 225 nm for 0.006 wt%, 0.01 wt%, 0.02 wt%, and 0.05 wt% C_{60} solution, respectively (Fig. 5.2(b-e)).
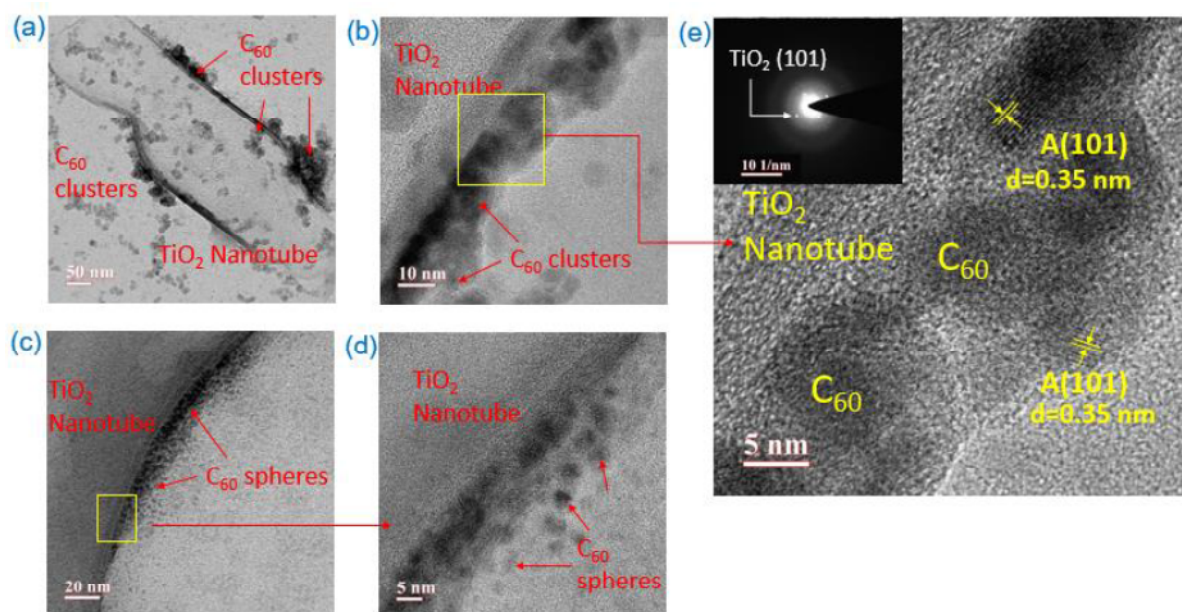
Fig. 5.3. Transmission electron micrograph (TEM) of C_{60}-functionalized TiO_2 nanotubes (S_3). (a, b) C_{60} clusters are decorated on the side wall of TiO_2 nanotubes. (c, d) Very small clusters and individual spheres of C_{60} attached on the wall of TiO_2 nanotube. (e) High resolution TEM (HRTEM) image of C_{60}-TiO_2 interface showing the lattice spacing of anatase TiO_2. SAED pattern in inset of figure (e).

FESEM image in Fig. 5.2(f-i) depicts the top surface decoration of C_{60} clusters on TiO_2 nanotubes. Hydrated fullerene-C_{60} molecules were aggregated and formed clusters of different dimensions as estimated in Fig. 5.2(b-e) and decorated on the top of the TiO_2 nanotubes. Owing to the decoration of individual and clustered C_{60}, surface roughness of the TiO_2 nanotubes were increased significantly as depicted in Fig. 5.2(f-i). Decoration of small and individual C_{60} spheres are completely invisible in the FESEM image in Fig. 5.2(f-i). Also, the decoration of C_{60} at the sidewall of the TiO_2 nanotubes is not evident from FESEM image. Therefore, a detailed TEM analysis was performed to figure out the decoration of small and individual C_{60} spheres on TiO_2 nanotube surface as shown in Fig. 5.3. However, the original morphology of TiO_2 nanotubes was not interrupted significantly after C_{60} functionalization, as confirmed from FESEM image in Fig. 5.2.

TEM image in Fig. 5.3(a) depicts the distribution of C_{60} clusters of different sizes over the surface of TiO_2 nanotubes. The closed view of C_{60}/TiO_2 interface in Fig. 5.3(b) indicates a uniform coverage of TiO_2 nanotube surface by C_{60} clusters having quite a small dimensions as compared to the average cluster size measured in Fig. 5.2(b-e). Fig. 5.3(c) and (d) show extremely small cluster size of C_{60} (< 5 nm) decorated to the TiO_2 nanotube surface. Size of a

few C_{60} spheres is closed to 1 nm that indicates the existence of individual C_{60} molecules in the composite. The highly crystalline nature of the TiO_2 nanotubes is authenticated from the discrete high-resolution spots with incomplete rings in the selected-area electron diffraction (SAED) pattern in the inset of Fig. 5.3(e). High-resolution TEM (HRTEM) image in Fig. 5.3(e) shows the C_{60}/TiO_2 interface where inter-planer distance of 0.35 nm corresponds to the anatase (101) crystal plane.

However, the TEM image undoubtedly confirms the enhancement of surface roughness and porosity of the TiO_2 nanotubes due to the surface functionalization by C_{60} of different clusters. But the TEM image can only show a very small area of samples that is insufficient to compare the overall surface area, the porosity of the composites having different concentrations of C_{60}. So, the overall surface area, average pore size, and pore volume of all the five samples (S_0-S_4) were estimated from the BET analysis.

BET analysis

Table 5.1: BET analysis of pure TiO_2 nanotube array and C_{60}-TiO_2 composites.

Sample	$a_{s\ BET}$ (m^2/g)	Pore Size (nm)	Pore Volume (cm^3/g)
Pure TiO_2NT (S_0)	1.74	28.36	2.466
C_{60}(0.006wt%)-TiO_2 (S_1)	2.54	25.9	3.3
C_{60}(0.01 wt%)-TiO_2 (S_2)	5.92	24.58	3.5
C_{60}(0.02 wt%)- TiO_2 (S_3)	19.36	5.79	4
C_{60}(0.05 wt%)- TiO_2 (S_4)	1.14	56.43	1.5

While the microscopic characterizations showed the morphological overview of the C_{60}-TiO_2 nanotube composites, BET analysis provided the quantitative detailing of the surface area (a_s), pore volume and pore size distribution of all the samples via nitrogen adsorption-desorption curve. N_2 was taken as the adsorptive and all the measurements were performed at 77 K. The surface area, pore size and pore volume of each samples are compared in Table 5.1. These results were aroused as the TiO_2 nanotubes exhibit high porosity which was enhanced further by the functionalization of C_{60} particles/clusters. As compared to the pure TiO_2 nanotubes (S_0), surface area (a_s) was increased gradually from S_1 to S_3 and decreased in the case of S_4 as shown in the Table 5.1. Therefore, S_3 (0.02 wt% C_{60}) exhibits highest surface area (a_s) of 19.36 m^2/g which is eleven times higher than the S_0. While the surface area increased from S_1 to S_3 with increase of the concentration of C_{60}, S_4 showed least surface area among all, possibly due to the excess intercalation of fullerene molecules into the pores of TiO_2 nanotubes and thereby reducing the overall surface area. Average pore size was found very less in S_3 as compared to

114

other samples whereas S_4 exhibited quite a large average pore size, possibly due to the aggregation of relatively large C_{60} clusters outside the TiO_2 nanotubes rather than entering into the porous structure as shown in the FESEM image in Fig. 5.2(i). Therefore, average pore volume was increased gradually from S_0 to S_3 and the lowest pore volume was calculated for the S_4.

Structural characterization

X- ray diffraction patterns were studied for all the samples and represented in Fig. 5.4(a). The sharp intensity peak near 25° confirmed the major contribution of anatase crystallinity (101) in all the five samples (S_0-S_4). However, a little increment of the rutile crystallinity in all the nanocomposite samples after hydrothermal treatment is shown in Fig. 5.4(a). Rutile (110) peak in all the nanocomposite samples is clearly visible near 28.8°. The low intensity peak at 36.1° and 68.2° in nanocomposite samples corresponds to rutile (101) and (301) crystallinity, respectively. Other anatase crystallinity peaks of (200), (105), (211) and (118) were observed at 35°, 53.5° 54.61° and 62.2°, respectively. All the other peaks labelled as "T" originated from titanium substrate. The existence of C_{60} in the nanocomposites is confirmed by the C (222) orientation of carbon at 20.4° in S_1-S_4 samples [24],[25].

Raman spectra (Fig. 5.4(b)) of all the samples were collected by using 600 nm laser at room temperature. The sharp peak at 144 cm^{-1} (E_g) and the low intensity peaks at 195 cm^{-1}(E_g), 395 cm^{-1}(B_g), 514 cm^{-1} (A_g+B_g) and 634 cm^{-1} (E_g) all accord with the anatase phase of TiO_2. The intensity of the E_g (144 cm^{-1}) peak is highest in pure TiO_2 nanotube sample and is decreased as per the increase of fullerene concentration in the nanocomposite. S_4 showed the lowest intensity in all the five active modes of TiO_2. The decreased intensity and broadening of peaks of the nanocomposite samples can be attributed to the formation of defects with increment of fullerene molecules due to the formation of covalent bonds between TiO_2 and C_{60} (Ti-O-C=O or Ti-O-C). In order to evaluate the presence of C_{60} in the nanocomposite a scan 1000 cm^{-1} to 1800 cm^{-1} was examined as shown in the inset of Fig. 5.4(b). A small intensity peak at 1450 cm^{-1}, observed in all the four nanocomposite samples (S_1-S_4) is attributed to the pentagonal pinch mode (A_g (2)) of C_{60} particles [26]. The second small peak at 1568 cm^{-1} is observed in samples with 0.02 wt % (S_3) and 0.5 wt% (S_4) of fullerene depicts the H_g (8) mode of C_{60} [26-28].
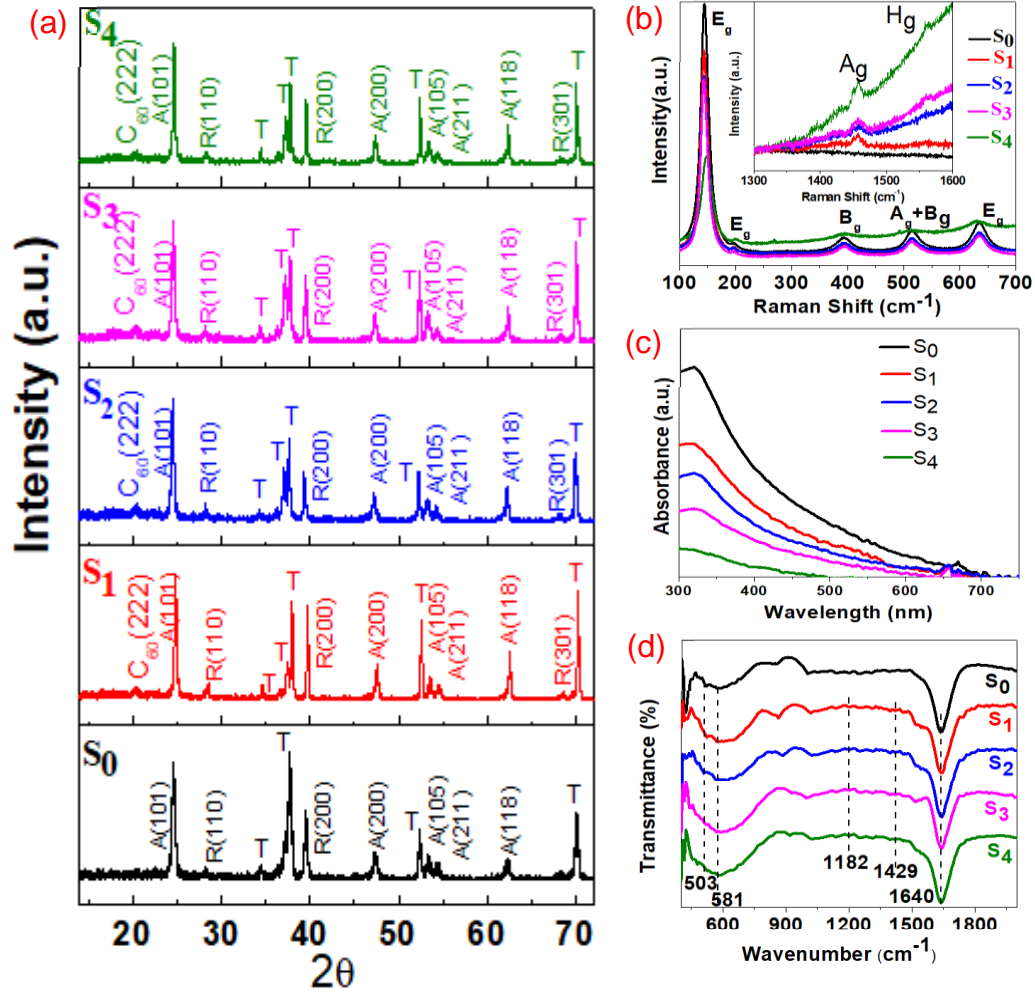
Fig. 5.4. Spectroscopic characterizations of all the samples (S_0-S_4). (a) XRD spectra, (b) Raman spectra, (c) UV Vis spectra, (d) FT-IR spectra.

UV Vis absorption spectra was recorded in-between 200 to 800 nm wavelength at room temperature (Fig. 5.4(c)). Absorbance spectra of the nanocomposite is more directed towards the TiO$_2$ nanotubes. Pure TiO$_2$ nanotube array (S_0) showed the adsorption edge near 403 nm which corresponds to the band gap of 3.08 eV. However, C_{60} has its adsorption edge in the UV region [20]. Therefore, upon formation of C_{60}-TiO$_2$ composites, the adsorption edge shifted towards the lower wavenumber i.e. in the UV region [23],[24]. S_1, S_2, S_3 and S_4 exhibited the adsorption edge near 406, 395, 388 and 388 nm. The bandgap is calculated from the following formula [29] where the absorption coefficient is associated to E_g as

$$\alpha h\nu = A(h\nu - E_g)^{1/2} \tag{5.3}$$

A is the constant and $h\nu$ is the incident photon energy and the calculated corresponding bandgap of samples are 2.9, 3.05, 3.13, 3.19 and 3.19 eV for S_0, S_1, S_2 S_3 and S_4, respectively. However, S_3 and S_4 nanocomposites showed approximately an equal bandgap around 3.19 eV.

116

Also, the absorbance of nanocomposite samples from S_0 to S_4 is decreased with an increment of fullerene concentration.

FTIR spectra of pure TiO_2 nanotube array and C_{60}-TiO_2 nanocomposite samples are represented in Fig. 5.4(d). Infrared active fundamental modes of anatase TiO_2 are principally located in-between the wavenumber of 400 to 1000 cm^{-1}. The band edges at 503 cm^{-1} and 581 cm^{-1} are attributed to the stretching vibration of Ti-O-Ti bonds and Ti-O bonds. After the formation of composite of TiO_2 with C_{60} (S_1-S_4), covalent bonds of Ti-O-C=O or Ti-O-C are formed and overall intensity increased as compared to the pure TiO_2 (S_0) [23],[24]. Strong absorption edge at 1640 cm^{-1} in all the samples is attributed to surface adsorbed water or hydroxyl groups. The bands representing internal modes of C_{60} are not very prominent in FTIR spectra (Fig. 5.4(d)) that indicates TiO_2 dominating feature of the composites. Low intensity band edges at 1182 cm^{-1} and 1429 cm-1 correspond to the internal modes of C_{60} in the composite [30]. The band edge at 3306 cm^{-1} corresponds to OH group (OH stretching) in all the samples (not shown in Fig. 5.4(d)).

Chemical characterization
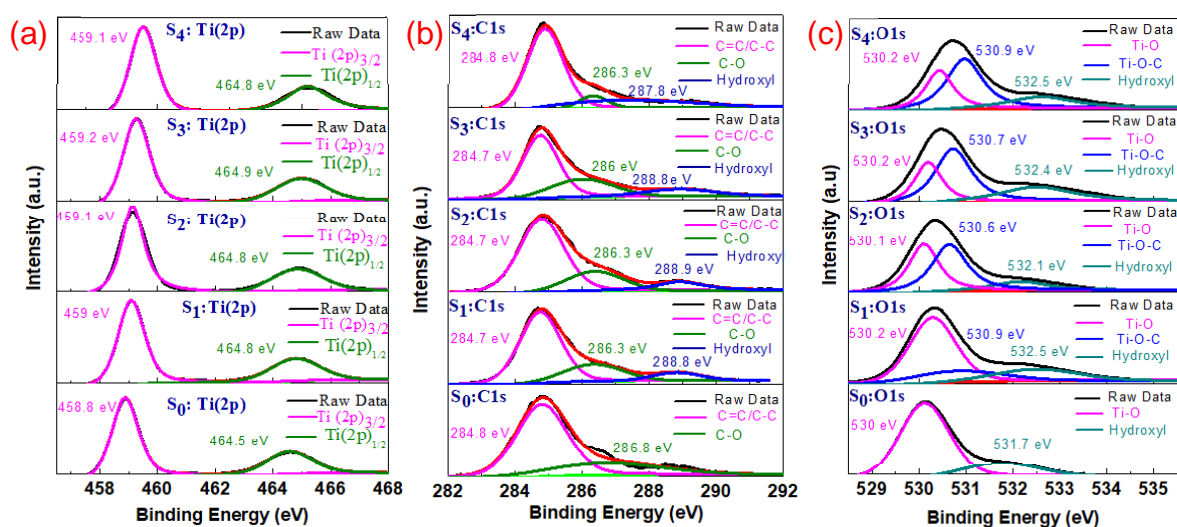
Fig. 5.5. Deconvoluted high resolution scan of X-ray photoelectron (a) Ti2p spectra (b) C1s spectra and (c) O1s spectra for all the samples (S_0-S_4).

The chemical state and composition of all the samples were examined with X-ray photo spectroscopy (XPS). The high resolution scan of Ti2p peak is shown in Fig. 5.5(a) and deconvoluted into doublet peaks of Ti2p$_{3/2}$ and Ti2p$_{1/2}$ at 458.8 eV and 464.5 eV respectively for all the samples (S_0-S_4). The separation of 6 eV between doublet peaks for all the samples authenticates the presence of anatase major in TiO_2 nanotubes [31].

To study the interaction of C_{60} molecules with TiO_2 nanotubes and the formation of covalent bond between the C_{60} and TiO_2, high resolution scans of C1s and O1s spectra were recorded. C1s spectrum in Fig. 5.5(b) of C_{60}-TiO_2 composites was deconvoluted into three sub-peaks near 284.7 eV, 286.3 eV and 288.8 eV. The highest intensity C1s peak at 284.7 eV corresponds to inherent carbon and sp^2 hybridized carbon of C_{60} [24],[32]. The broad peak near 286.3 eV is assigned to the defect containing sp^2 hybridized carbon from C_{60}. The peak is relatively weekend from S_1 to S_4 and thereby determining the decrease of the defects due to the surface adsorption of different oxygen species and hydroxyl ions to the C_{60} surface. The acute peak at 288.8 eV is aroused due to the presence of carbonyl group (C=O or C-O) and other surface functional groups which provides active sites for interconnection with TiO_2.This peak confirms formation of covalent bond (Ti-O-C) between the C_{60} and TiO_2 [30]. The area of this acute peak at 288.8 eV is increased from S_1 (0.006 wt%) to S_4 (.05 wt%) due to the simultaneous increase of fullerene concentrations.

The high resolution O1s spectra of pure TiO_2 nanotube exhibited one sharp peak near 530 eV and another small peak near 531.7 eV which are attributed to the chemically bonded lattice oxygen (Ti-O) and adsorbed surface oxygen groups, respectively [33],[34]. O1s spectra of all the nanocomposites (S_1-S_4) were deconvoluted in three peaks near 530.2 eV, 530.7 eV and 532 eV (Fig. 5.5(c)). The additional peak at around 530.8 eV is aroused in all the nanocomposites which confirms the formation of Ti-O-C linkage. The area of the peak at 530.8 eV is increased from S_1 to S_4. Also, the relative percentage area calculated for adsorbed surface oxygen (532 eV) to lattice oxygen (530.2 eV) was increased with the increment of fullerene-C_{60} concentrations and exhibited 20%, 37%, 59%, 72 % and 69%S_0 for S_0, S_1, S_2, S_3, and S_4, respectively. Therefore, S_3 (0.02 wt %) depicted the highest peak intensity at 532.8 eV and highest surface oxygen percentage of 72%.

5.2.3 Device fabrication

Metal-Insulator-Metal (MIM) structured sensors were fabricated with Au and Ti as the top and the bottom electrodes. ~150 nm thick Au top electrodes were deposited on C_{60} decorated TiO_2 nanotubes/Ti samples by using electron beam evaporation technique. Molybdenum metal shadow masks were used to develop 1.5×1.5 mm^2 Au top electrodes. Then the samples were sliced into small pieces and the Ti metal (bottom electrode) was exposed by selective HF etching of oxide layers. Also the device fabrication techniques have been describe in chapter 1 and chapter 3.

5.2.4 VOC sensing

Figure 5.6 exhibits all the five sensors (S_0 to S_4) in the exposure of 100 ppm of formaldehyde at 150°C. Pure TiO_2 nanotubes (S_0) showed a 58.24% response magnitude with an extended response and recovery time. On the other hand, functionalized C_{60} decorated all the TiO_2 nanotube sensors showed response magnitude more than 89% in 100 ppm formaldehyde at 150°C. So, the current results undoubtedly confirm the remarkable improvement of the VOC sensing performance of TiO_2 nanotubes array after incorporation of fullerene C_{60}. The response magnitude and the response/recovery characteristics improved significantly in C_{60}-TiO_2 nanotubes sensors. Among all the C_{60} decorated TiO_2 nanotube sensors, S_4 exhibited highest response magnitude of 99.6% where S_3 exhibited the fastest response and recovery characterized towards 100 ppm of formaldehyde at 150°C (Fig. 5.6).
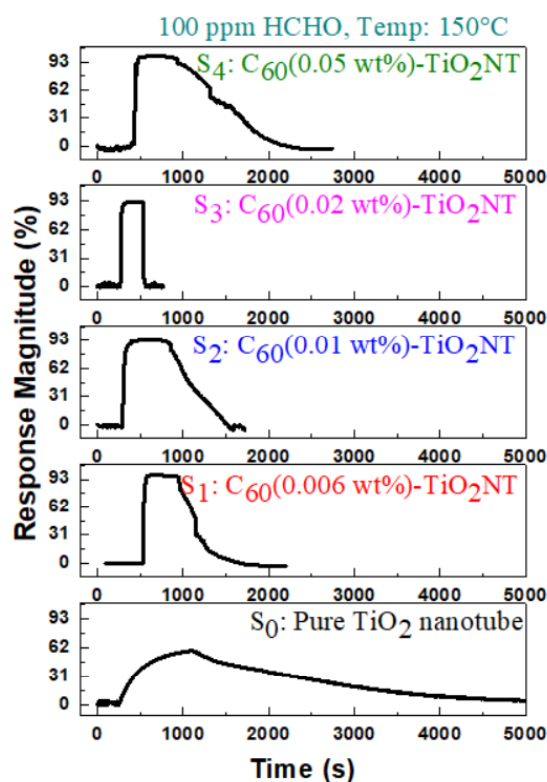
Fig. 5.6. Comparative response of all the five sensors (S_0-S_4) in the exposure of 100 ppm formaldehyde at 150 ℃.

All the C_{60}-TiO_2 composite sensors were examined at four different temperatures i.e. 50°C, 100 ℃, 150°C and 200°C in the exposure of 100 ppm formaldehyde and shown in Fig. 5.7(a-d). While, S_1, S_3 and S_4 showed the highest response magnitude at 150 ℃, S_2 revealed the highest response magnitude at 100 ℃. In terms of response magnitude, S_4 was considered to be the best as it had shown the excellent response magnitude ∼ 66 %, 94 %, 99.9 % and 98 %

towards 100 ppm of formaldehyde at 50 °C, 100 °C, 150 °C and 200 °C, respectively. Even at 50°C, all the nanocomposite sensors exhibited appreciably high response magnitude of 28 %, 40 %, 32 % and 66 % for S_1, S_2, S_3 and S_4, respectively. The represents the response magnitude of S_1-S_4 sensors was saturated/decreased at the elevated temperature (>150 °C) as shown in Fig. 5.7(e). So, 150 °C was considered as the optimized temperature for further study. The saturation of response magnitude at high temperature can be attributed to the kinetics mechanism behind the adsorption and desorption of reducing vapours on the surface of the nanocomposite. At very low room temperature, vapour/gas molecules depicts slow kinetics which in turn leads to low response magnitude. At a very high temperature, the vapour/gas molecules getaway before interacting with the target sites on the surface of the nanocomposite due to high kinetics resulting in the decrement of response magnitude [35-37].
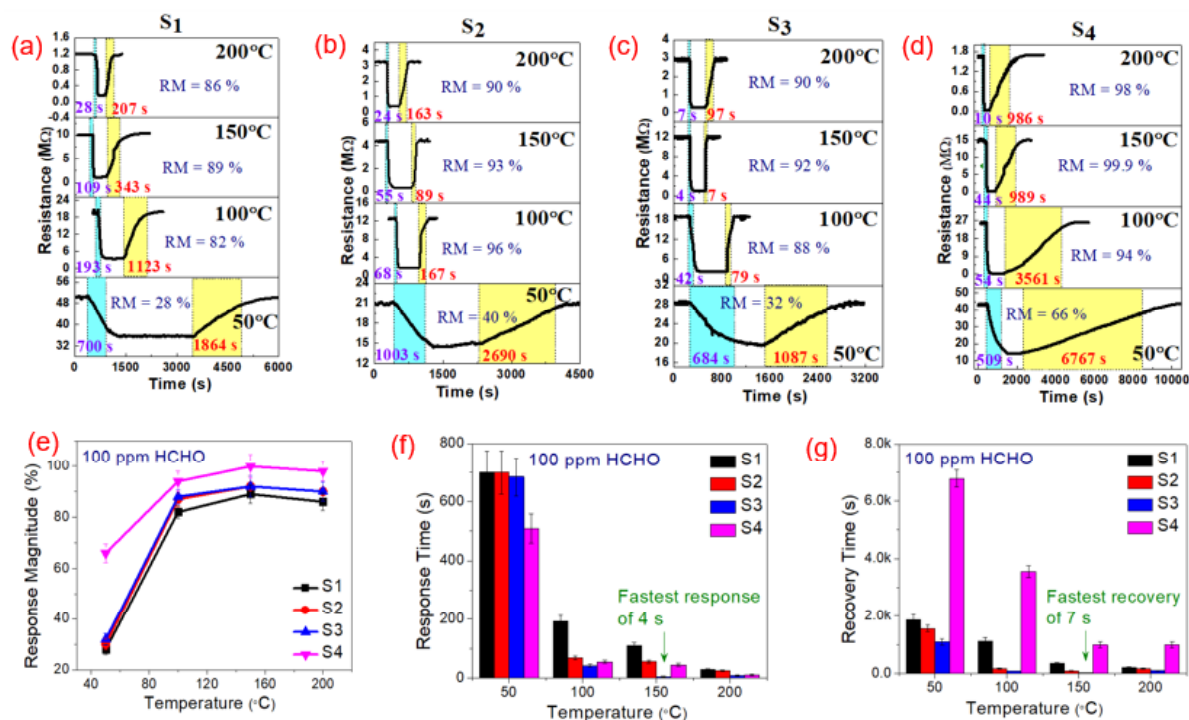
Fig.5.7. Temperature effect on the transient behaviour of C_{60}-TiO_2 composite sensors i.e. (a) S_1, (b) S_2, (c) S_3 and (d) S_4. (e) Response magnitude, (f) response time and (g) recovery time as a function of temperature for S_1-S_4.

Response and recovery time of S_1-S_4 sensors were calculated at all four temperatures where a gradual improvement in response/recovery characteristics was observed at the elevated temperature Fig. 5.7(f, g). S_3 was fastest among all the nanocomposite sensors and showed ultra-fast response and recovery time of ~ 4 s and ~ 7 s at 150 °C, respectively (Fig. 5.7(f, g)). S_1 and S_2 also showed substantially fast response/recovery time of 109 s/343s and 55s/89s, respectively at 150 °C. S_4 took the exceptionally longest time to recover (989 s at 150 °C). It

has been depicted with many reports that excess-carbon-based nanocomposites have slow recovery in exposure to different VOC's or other toxic gasses [38],[39]. The excess amount of fullerene in the nanocomposite can improve the sensitivity but elongates the recovery time. Considering all the three performance parameters i.e. response magnitude, response and recovery time, S_3 was considered as the best performing sensors among all. Appreciably high response magnitude (92 %) and ultra-fast response/recovery (4 s/7 s) characteristics towards 100 ppm HCHO at 150 ℃ make S_3 superior to any other sensors.
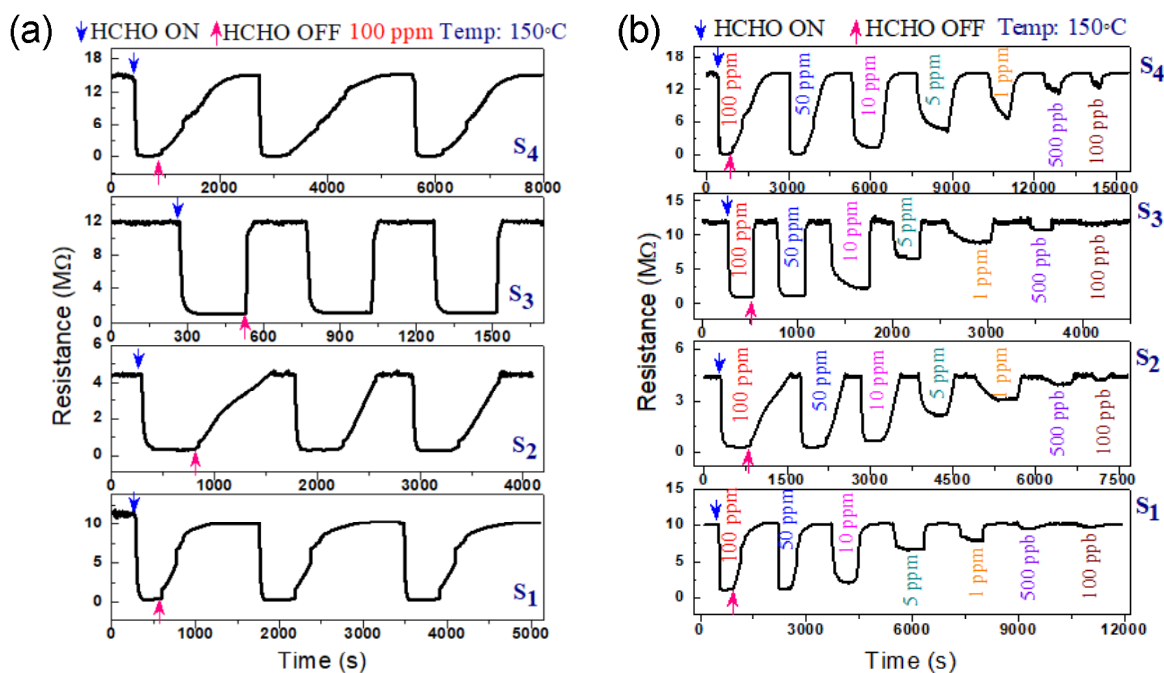

Fig. 5.8. (a) Repeated cycles measured in 100 ppm formaldehyde, (b) transient behaviour within the range of 100 ppb to 100 ppm at 150 ℃ for all the C_{60}-TiO_2 nanotube sensors.

All the C_{60}-TiO_2 nanotube sensors (S_1-S_4) exhibited quite a stable baseline resistance with highly repeatable transient behaviour at throughout the temperature range (50 to 200 ℃) in the exposure of air as well as VOCs like formaldehyde. All the sensors returned to its actual baseline resistance after being exposed to VOCs. All the sensors (S_1-S_4) showed the baseline resistance in mega ohms range at room temperature and reduced significantly at the elevated temperature (Fig. 5.8). The repeated cycle study for all the four sensors (S_1-S_4) was performed in the exposure of 100 ppm formaldehyde at 150 ℃, as represented in Fig. 5.8(a).

Transient response was measured for all the C_{60}-TiO_2 composite sensors for the seven different concentrations like 100 ppm, 50 ppm, 10 ppm, 5 ppm, 1 ppm, 500 ppb and 100 ppb of formaldehyde at 150 C as shown in Fig. 5.8(b). Successful detection of lower ppb concentration of formaldehyde was an important feature of the fullerene decorated TiO_2 nanotube sensors. Response magnitude of all the sensors showed an almost equal response at

121

100 and 50 ppm and gradual decrement below 50 ppm of concentrations. This result confirms the greater applicability of the sensors to detect very low concentrations (50 ppm to lower ppb level) of HCHO.
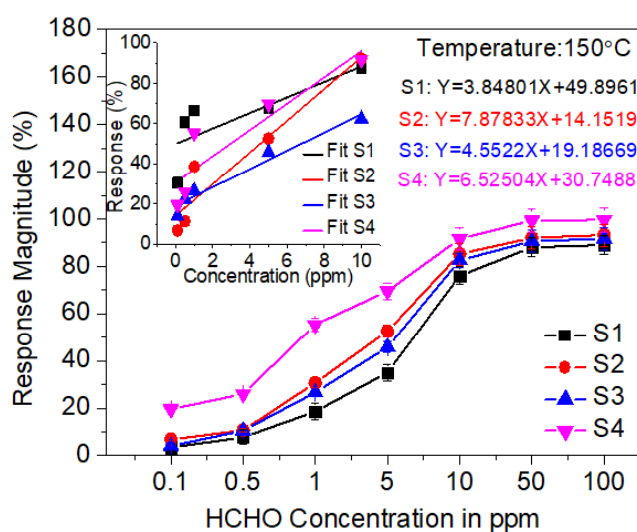

Fig. 5.9. Response magnitude as a function of the concentrations of formaldehyde.

Response magnitude as a function of HCHO concentrations from Fig. 5.8(b) is represented in Fig. 5.9. Fig. 5.9 clearly envisages the saturated response above 50 ppm of formaldehyde for all the sensors. However, gradual decrement of response magnitude is noticed below 50 ppm of concentrations of HCHO in Fig. 5.9. The linear dependency of the response magnitude of S1-S4 was estimated in the inset of Fig. 5.9 under the HCHO concentration range of 0.1 ppm to 10 ppm. The fitted straight line equations for all the four sensors are listed in Fig. 5.9 where x represents the concentration of HCHO and y represents the response magnitude. The correlation coefficient R^2 was measured as 0.62147, 0.911911, 0.96109 and 0.83715 for S_1, S_2, S_3 and S_4, respectively. Among all the four sensors, S_3 exhibited promising linear dependency (R^2=0.96109) confirming its applicability towards quantitative detection of formaldehyde at low concentration range (0.1 to 10 ppm). So, S_3 was treated as the best performing sensor in terms of linear dependency of response as a function of the HCHO concentration and further selectivity and humidity study was carried out with S_3 sensor only.

S_3 sensor was tested with different groups of volatile organic compounds (VOCs) like alcohols (2-propanol), aldehyde (formaldehyde), alkanes (pentane), ketone (acetone) and aromatic hydrocarbon (toluene, benzene, xylene) to assess its selective behaviour as shown in Fig. 5.10(a). Therefore, all the C_{60}-TiO_2 nanotube composite sensors exhibited very high response towards aldehyde and where S_3 (i.e. 0.05 wt% C_{60}-TiO_2) showed 92 %, 67 % and 45 % response towards 100 ppm of formaldehyde, pentane and acetone at 150 ˚C, respectively (Fig. 5.10(a))).

C_{60}-TiO_2 nanotube composite sensors were considered selective towards formaldehyde, considering the highest natural response towards formaldehyde.
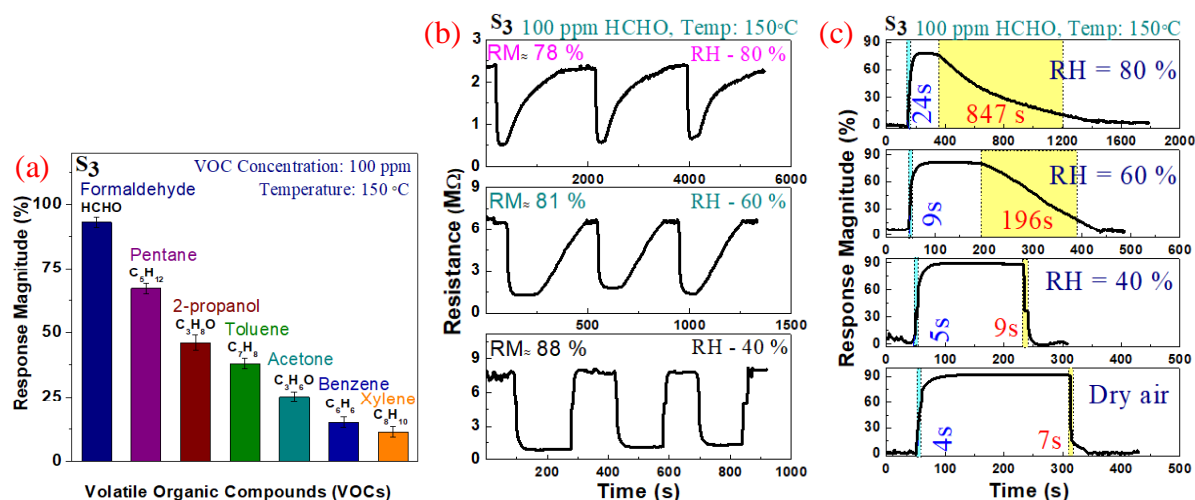
Fig. 5.10. (a) Bar chart representing the magnitude of S_3 in the exposure to different VOCs to asses formaldehyde selective nature of the sensor, (b) transient behaviour under different relative humidity (40% - 80%), (c) Comparative response in dry air and different humid conditions with measured response and recovery time for S_3 in 100 ppm of formaldehyde at 150 ˚C.

The response of S_3 was tested under different humid environment (40 % to 80 %) at 150 ˚C and depicted in Fig. 5.10(b, c). The relative decrease in the response magnitude was observed with the increase in the humidity. A significant lowering of response magnitude was observed under humid conditions. 92%, 88%, 81% and 78% response were recorded for S_3 under dry, 40%, 60% and 80% RH environment, respectively. A significant increment in response and recovery time was also noticed in the presence of elevated RH levels (Fig. 5.10(c)). Response/recovery time for S_3 was measured as 4s/7s, 5s/9s, 9s/196s and 24s/847s in the presence of 40%, 60% and 80% RH in 100 ppm formaldehyde at 150 ˚C. The slow response and recovery characteristics are apparent from the repeated cycle and transient behaviour in Fig. 5.10(b) and (c).

At elevated RH, the resistance of the sensor in air ambient is decreased as the water vapours dominate over the surface of the sensor. In air ambient, the hydroxyl group (OH^-) from the water molecules gets adsorbed to the nanocomposite surface which in turn decreases the surface interaction sites for formaldehyde. The chemisorption of oxygen groups and formaldehyde molecules is hindered with increase in the humidity or an increase in the amount of hydroxyl group on the sensor surface. This causes a decrement in the response magnitude and increment in the response time and recovery time [40],[41].

5.2.5 Sensing mechanism

Ultra-high sensitive detection of formaldehyde by the functionalized C_{60} decorated TiO_2 nanotube based MIM structured sensors was principally governed by the enhanced surface area along with the increased interacting sites to react with the targeted gas/VOC molecules. Effective surface area of the highly porous TiO_2 nanotubes was further enhanced by the optimized insertion of spongy and nanoporous clusters of fullerene [21]. Whereas the surface interaction sites were increased significantly due to the presence of individual/clustered fullerene-C_{60} which was already functionalized with large number of oxygen functional groups. Consequently, the enhanced surface area and the existence of large surface oxygen both were authenticated by the BET analysis and XPS study in the materials characterization part, respectively.

The work function of C_{60} (~4.71 eV) [42] is significantly lower than the work function of anatase TiO_2 (~5.1 eV) [43] and electrons are transferred from lowest unoccupied molecular orbital (LUMO) of C_{60} to the conduction band of TiO_2 due to this work function difference upon formation of heterojunction between C_{60} and TiO_2. The excess electrons to the TiO_2 nanotube surface take part in the formation of the ionic species of oxygen species like O-, O^{2-} etc. as shown in the Fig. 5.11(a) and increase the surface reactivity of the nanotubes. At the same time, excess electrons transferred from C_{60} to the TiO_2 nanotube surface lowered the overall resistivity of the sensors. As a result, all the nanocomposites samples depicted resistance within the range of 21 MΩ– 45 MΩ while pure TiO_2 nanotube array depicted a resistance of 90 MΩ in room temperature.

Fullerene is considered as an electron-rich material and its electron concentration is altered significantly due to the surface adsorption/desorption of oxygen functional groups [11]. In the current study, hydrated fullerene (or fullerol) was decorated to the TiO_2 nanotube surface in form of the clusters of different sizes. Hydrated fullerene was then formed covalent bond with TiO_2 developing high quality nanocomposites $[Ti - OC_{60}(OH)_{x-1}]$. Further heat treatment in air ambient enhanced the number of reactive oxygen species (O_2^-, O^- and O^{2-}) to the fullerene surface, reducing the hydroxyl ions as discussed in section 5.2.1. The triply degenerate low-lying LUMO and the delocalized π structure of C_{60} enables the easy movement of electrons from TiO_2 to C_{60} [23],[24]. In air ambient, electron concentration in C_{60} is decreased due to the availability of the oxygen species in large number. However, electron deficiency in C_{60} extracts electron from TiO_2 nanotubes, increasing the width of surface depletion region (W) as shown in the Fig. 5.11(b). Electron depleted region is created both inner and outer sides of the

nanotubes and vertical electron transport occurs through the conducting channel (t) inside the nanotubes (Fig. 5.11(a, b)) [33].
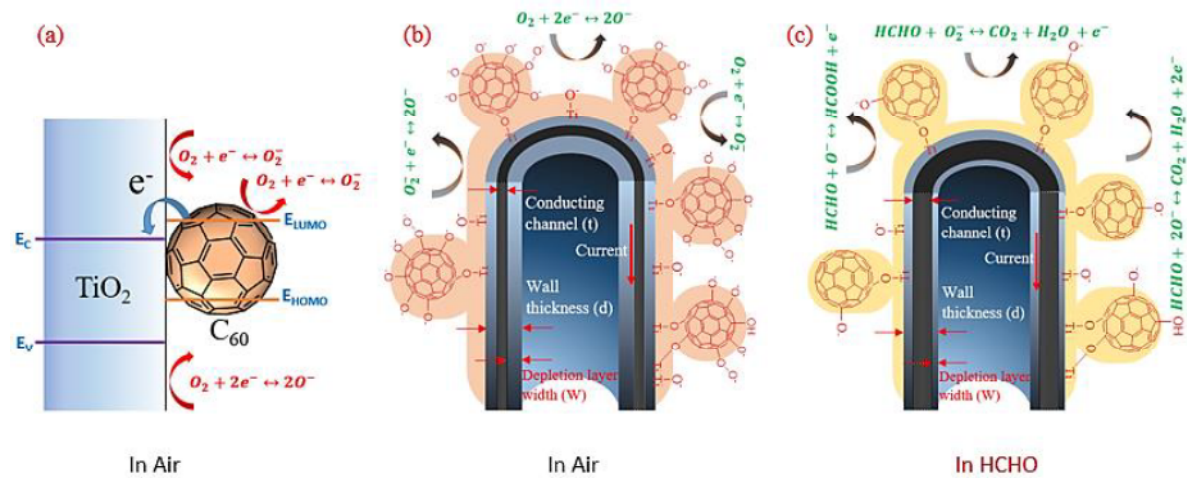
Fig. 5.11. (a) Energy band diagram of C_{60}-TiO_2 composite indicating possible electronic exchange in air ambient. Possible surface reactions in C_{60}-TiO_2 composite (b) in air ambient, (c) in presence of formaldehyde vapours.

In Au/C_{60}-TiO_2 nanotubes/Ti (MIM) structure, current principally flow through the conducting channel (t) due to applied bias as shown in the Fig. 5.11(b,c) [44],[45]. In air ambient, oxygen species are directly adsorbed to the TiO_2 Surface (Fig. 5.11(a)) or adsorbed to the interaction sites of C_{60} (Fig. 5.11(b)). However, both the process extract free electron from the TiO_2 surface and increases the depletion layer width (W) and reduces the effective width of the conducting channel (t) that eventually restrict the one dimensional (1D) current flow in Au/C_{60}-TiO_2 nanotubes/Ti sensors in air ambient [25]. On exposure to the formaldehyde vapours, the trapped electrons by reactive oxygen species are released to the nanocomposite surface. As a result, width of the depletion layer and the conducting channel in TiO_2 nanotubes is decreased and increased, respectively and one dimensional electron flow in the TiO_2 nanotube is increased as shown in Fig. 5.11(c).

C_{60} clusters provide a large number of interaction sites and thereby enhancing the overall surface reactivity of the nanocomposite. Due to high porosity of fullerene, its clusters are spongy in nature which causes the insertion of VOC's into the clusters. The communication of VOC with C_{60} molecules leads to the formation of weak ionic bonding that causes the localization of VOC molecules in C_{60} clusters [21]. C_{60} particles act as the reaction centres or active points and interact competently with the formaldehyde molecules and thereby smoothing the movement of electrons. C_{60} being an excellent electron reservoir shuttles electron from TiO_2 and then the release of electrons back to nanocomposite surface on exposure to formaldehyde vapours. Hence causing the increase in the conductivity and n type sensor

response for all the synthesized nanocomposite sensors. C_{60} lowers the barrier between the formaldehyde molecules and the TiO_2 nanotubes [46],[47]. The immense increase in the surface area and high surface reactivity provided by the C_{60} particles and clusters is responsible for high response magnitude of all the composite sensors with fast response time and recovery time.

Therefore, fullerene on the TiO_2 surface can enhance the effective surface area, average pore volume, adsorption possibility of the target species and easy movement of electrons between TiO_2 and C_{60}. All these factors together can be considered as the key reason behind the enhancing of the change of current in-between air and VOC ambient that eventually shows ultra-high sensitivity towards formaldehyde by the C_{60} functionalized TiO_2 nanotube-based sensors.

C_{60} concentration being varied from 0.006 to 0.05 wt% to synthesize the composites with TiO_2 nanotubes. As the microscopic study focused on a small area, the overall distribution of fullerene clusters on TiO_2 nanotube surface are not clearly been observed from the FESEM and TEM images to differentiate the morphology of the composites having different concentrations of C_{60}. So, the superiority of the S_3 as compared to any other composites was justified from the quantitative overview of the surface area, pore size, and pore volume obtained from the BET analysis. So, the functionalization of 0.02 wt% C_{60} (S_3) was considered as the optimized one that eventually showed the overall best performance in terms of response, recovery and linearity behaviour.

There are many factors deciding the selectivity of a sensing material towards a particular gas/VOCs. These factors mainly include morphology of the nanomaterials, redox states, surface area, pore structure, the content of surface oxygen species, catalytic activity of the nanomaterials surface etc. [48],[49]. Formaldehyde is an organic polar molecule having very small effective size of ~2.5 Å [50]. Efficient adsorption of formaldehyde molecules by using activated carbons nanoforms (such as activated carbon fibres) are well reported in the previous literature [50-54]. Large specific surface area, enhanced pore volume and large number of active sites in the sensing materials enhance the adsorption capacity of the formaldehyde [51], [52]. If the size of the micro/nanopores of the absorbent are closed to the effective size of the target adsorbate, selective adsorption is enhanced significantly [52],[53]. However, C_{60} functionalized TiO_2 nanotubes most probably achieved such desired porosity level to enhance the selective adsorption of VOC molecules having small kinetic size such as formaldehyde. Also, the overlapping of adsorbed molecule interaction from opposite wall of the extremely small pores induced significant enhancement of the adsorption of formaldehyde even at low

concentration (ppb level). The possible reactions between formaldehyde and adsorbed oxygen species to the nanocomposite surface are shown in Fig.5.11(c).

5.3 Fullerene-C_{60} encapsulated TiO_2 nanoparticles

5.3.1 Synthesis
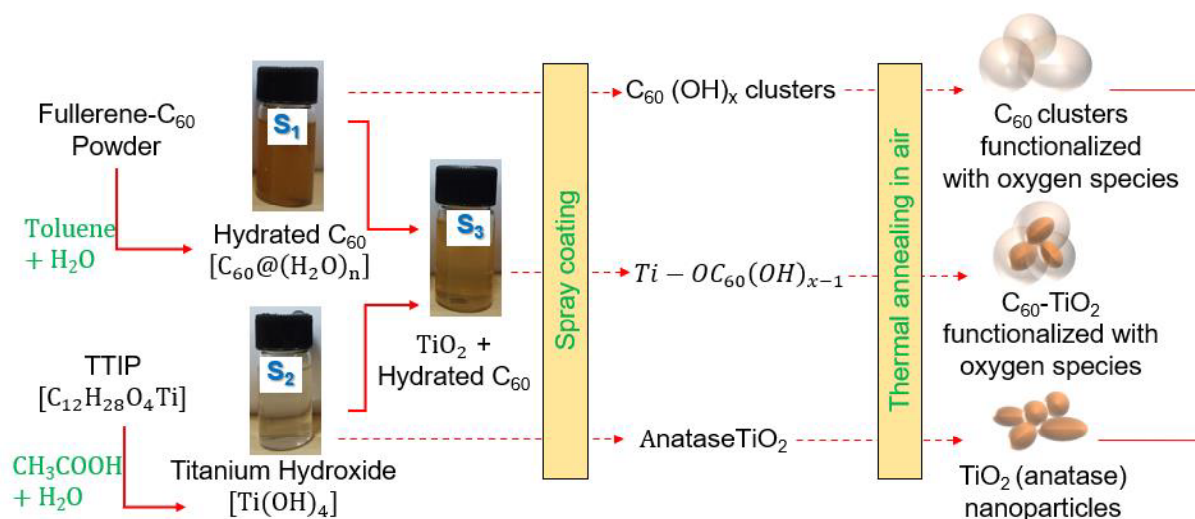
Fig. 5.12. A flow diagram to show the synthesis and fabrication steps of the pure C_{60}, TiO_2 nanoparticles (NP) and C_{60}-TiO_2 composite sensors.

The process to synthesize the TiO_2 nanoparticles has been previously discussed in earlier chapter 2. The process to functionalize or oxide the fullerene molecules to develop their hydrophilicity has been described in detail in the above section (5.2.1). 0.01 wt% of aqueous fullerene solution was prepared for the formation of nanocomposite. The C_{60}-clusters encapsulated TiO_2 nanoparticle was synthesized by mixing both the solutions in equal volume followed by a sonication for one hour (Fig. 5.12).

Formation of oxygen functionalized C_{60} encapsulated TiO_2 nanoparticles

The functionalized C_{60} particles and clusters having abundant oxygen species were encapsulated around TiO_2 nanoparticles in the same way as described in the above section 5.2.1. A large number of functionalized C_{60} is connected to the Ti atoms (via oxygen) and forms fullerene encapsulated TiO_2 nanoparticles hybrid. The coverage of C_{60} molecules over TiO_2 nanoparticles enhances the stability as well as the reactivity of the hybrid. During the synthesis of hybrid, hydrated fullerene forms covalent bond with titanium hydroxide [Ti(OH)$_4$] as shown in Fig. 5.12.
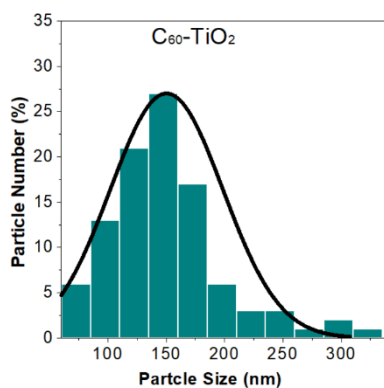
5.3.2 Characterization

Morphological characterization
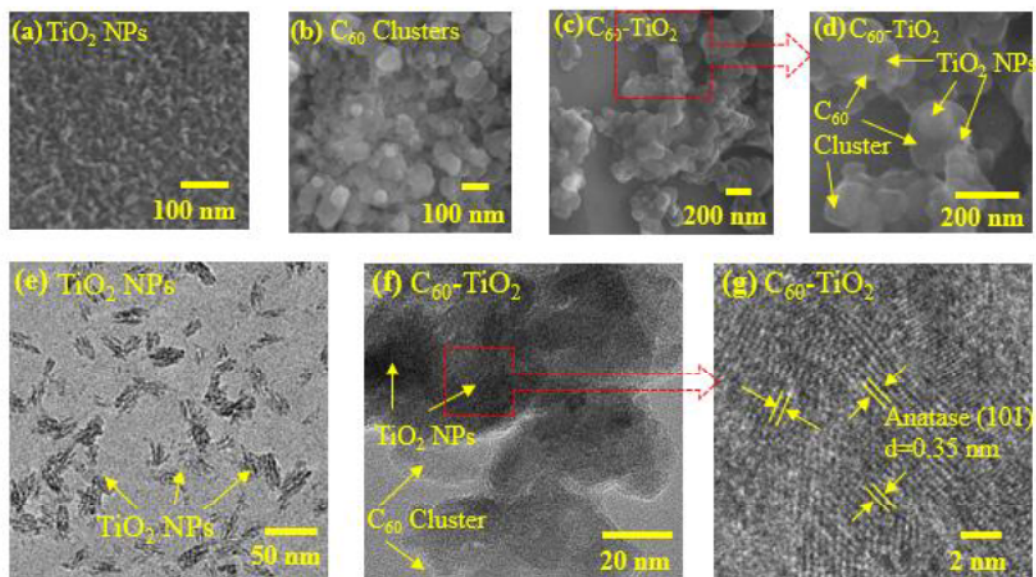
Fig.5.13. FESEM images of (a) pure TiO_2 nanoparticles (S_2), (b) fullerene-C_{60} clusters (S_1), (c, d) C_{60}-TiO_2 nanohybrid (S_3). TEM image of (e) TiO_2 nanoparticles and (f) TiO_2 NPs encapsulated in fullerene-C_{60} clusters (S_3). (g) HRTEM image of the C_{60}-TiO_2 nanohybrid (S_3) indicating the existence of anatase (101) crystallinity with lattice spacing of 0.35 nm.

Fig. 5.12(a-d) shows the FESEM image of three different types of samples. Dense and uniform layer of TiO_2 nanoparticles is observed in Fig. 5.13(a). Isolated nanoparticles of TiO_2 having diameter in-between 10-35 nm are clearly visible in the TEM image in Fig. 5.13(e). Fig. 5.13(f) exhibits the closed view of the C_{60} encapsulated TiO_2 nanoparticles where the boundary layer of C_{60} adjacent to the TiO_2 nanoparticles is clearly noticeable. The high resolution TEM image in Fig. 5.13(g) revealed anatase (101) crystallinity of the TiO_2 with lattice spacing of 0.35 nm. Pure C_{60} clusters were almost circular in shape with different sizes of 50-350 nm (Fig. 2.13(c)). The size distribution in Fig. 2.13(c) indicates 161 nm of average size of the C_{60} clusters.

The average size of the TiO_2 nanoparticles is 18 nm which is depicted in Fig. 2.8 of chapter 2. C_{60}-encapsulated TiO_2 nanoparticles are also circular in shape and mostly connected with each other as shown in the Fig. 5.13(c) and (d). Size distribution in Fig. 5.14 exhibits the average size of 150 nm for C_{60}-encapsulated TiO_2 that confirms the reduction of the C_{60} cluster sizes after formation of nanocomposite.

Fig. 5.14. Size analysis of C_{60}–encapsulated TiO_2 NPs.

Structural characterization
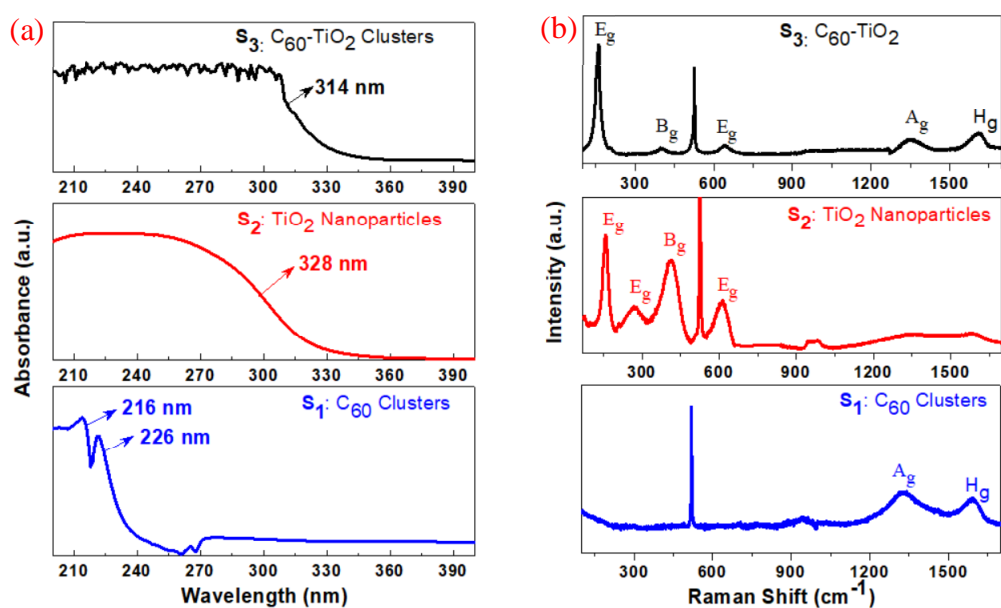
Fig. 5.15. Spectroscopic characterizations of all the samples. (a) UV vis adsorption spectra, (b) Raman spectra.

The UV Vis absorption spectra in Fig. 5.15(a) exhibits two broad absorption edges for C_{60} clusters in the UV region at 216 nm and 226 nm [15]. These optical absorption bands are recognised as dipole allowed transitions in original C_{60} and are accordant with literature [1],[55]. Pure TiO_2 nanoparticle shows the adsorption edge near 330 nm indicating quite a high optical bandgap of 3.78 eV which can be considered a well resembling band gap for the ultra-small TiO_2 nanoparticle. Upon formation of a composite of TiO_2 nanoparticles with C_{60} clusters, the absorption edge was shifted to the 314 nm indicating almost 3.94 eV optical bandgap (Fig. 5.15(a)).

Raman spectroscopy scan from 50 to 2000 cm^{-1} was performed using 500 nm laser at room temperature for all the three samples and shown in Fig. 5.15(b). The active Raman modes of

E_g (144 cm^{-1}), E_g (199 cm^{-1}), B_g (399 cm^{-1}), A_g (516 cm^{-1}) and E_g (639 cm^{-1}) in pure TiO$_2$ nanoparticle (S$_2$) and C$_{60}$ encapsulated TiO$_2$ (S$_3$) corresponds to anatase crystallinity [21]. The presence of C$_{60}$ is authenticated from the A_g and H_g peaks observed in C$_{60}$ encapsulated TiO$_2$ (S$_3$) and pure C$_{60}$ clusters (S$_1$). Also, the Raman modes for TiO$_2$ within the range of 100 to 1000 cm^{-1} are absent in the S$_1$ sample. The formation of Ti-O-C linkages with the transfer of electrons from TiO$_2$ to C$_{60}$ is recognised by the shifting of pentagonal pinch mode (A_g) towards higher wavenumber (red shift) (Fig. 5.15(b)) [16],[56]. A high intensity peak at 525 cm^{-1} is observed in all the three samples corresponding to Silicon, originated from the Si/SiO$_2$ substrate [57].

Chemical characterization
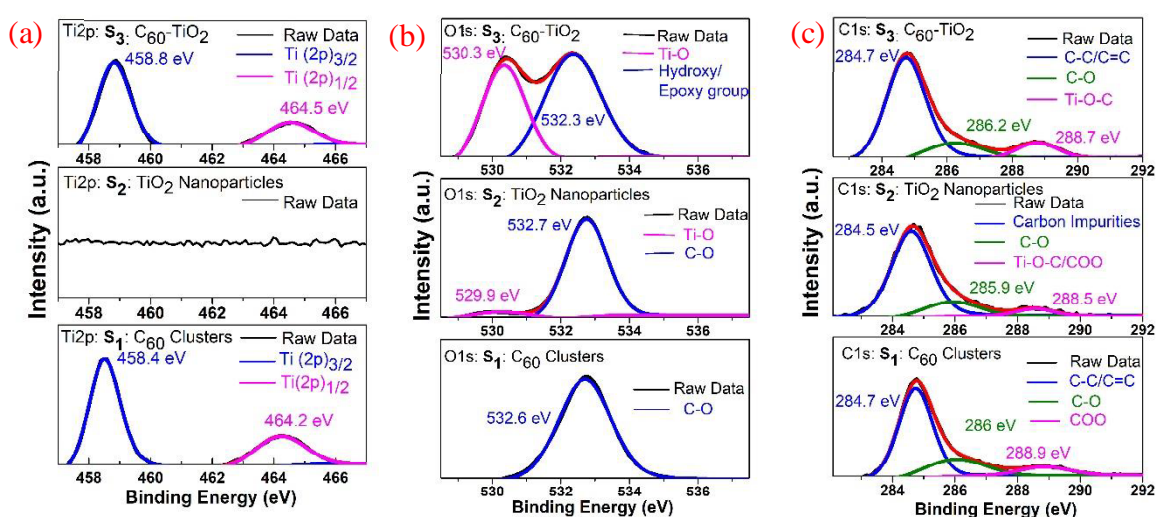
Fig. 5.16. XPS spectra with high resolution scan of (a) Ti2p, (b) O1s, (c) C1s peaks.

The high resolution Ti2p XPS scan of all the samples (S$_1$-S$_3$) is depicted in Fig. 5.16(a). The Ti2p spectra is showing the doublet peaks at 458.4 eV and 464.2 eV for S$_2$ and S$_3$. The separation of 6 eV between two doublets confirms the anatase crystallinity of the TiO$_2$ nanoparticle. S$_1$ i.e. pure C$_{60}$ does not display any peak in the Ti2p scan [33].

The O1s spectra of pure TiO$_2$ nanoparticles (S$_2$) showed a high and low binding energy peak at 532.7 eV and 529.9 eV respectively (Fig. 5.16(b)). The high binding energy peak (532.7 eV) corresponds to the organic impurities and adsorbed surface oxygen groups [34]. The low binding energy peak (529.9 eV) corresponds to the lattice oxygen. However, due to the ultra-small size of the TiO$_2$ nanoparticles, effective surface area is quite high in TiO$_2$ NPs that justify the large area peak at 532.7 eV and very small area peak at 529.9 eV. C$_{60}$ encapsulated TiO$_2$ NP exhibits quite a high area in the low binding energy bulk oxygen peak (530.3 eV)

confirming the accumulation of TiO_2 nanoparticles (Fig. 5.16(a) and (b)) after the formation of composite (S_3). The large area of surface oxygen peak at 532.3 eV indicates the presence of a high amount of hydroxyl, epoxy and other oxygen species that are aroused due to the C_{60} boundary surrounding the TiO_2 nanoparticles (Fig. 5.16(b)). Only a high binding energy surface oxygen peak near 532.6 eV in pure C_{60} clusters confirmed the existence of a large number of surface oxygen groups due to the functionalization of fullerene molecules [57],[58]. The use of organometallic salt (TTIP) and acetic acid in the synthesis of TiO_2 nanoparticle (S_2) by sol gel method gave rise to different carbon impurities which further led to the rise of two high intensity peaks at 284.5 eV and 285.9 eV in C1s scan in Fig. 5.16(c). A small intensity peak at 288.7 eV depicts the formation of carboxyl group or Ti-O-C linkage in the pure TiO_2 nanoparticles. The high resolution C1s peak of pure C_{60} cluster (S_1) and C_{60}-encapsulated TiO_2 NPs hybrid (S_3) was deconvoluted into three peaks located at 284.5 eV, 286 eV and 288.9 eV (Fig. 5.16(c)). The high intensity peak at 284.5 eV is the contribution of the sp^2 hybridized carbon atoms observed in both the samples i.e. S_1 and S_3. The relatively low intensity peak at 286 eV corresponds to the oxidized carbon which is aroused due to defects in the sp^2 hybridized carbon [16]. The right most peak at 289 eV in S_1 is assigned to the carbonyl group (O=C-O) that originated due to the functionalization of fullerene molecules. The increase in the area of the peak at 288.7 eV in S_3 as compared to S_1 and S_2 confirms the formation of Ti-O-C linkage indicating good quality hybrid formation [20],[59].

5.3.3 Device fabrication

Three planar types of sensors were fabricated by using three different precursors i.e. (i) hydrated fullerene-C_{60} (S_1), (ii) TiO_2 nanoparticles (S_2) and (iii) C_{60}-TiO_2 composites (S_3). Then the three types of sensors were annealed in air ambient for 5 hours at 250 °C to enhance the mechanical and electrical stability of the sensing layer. Au electrodes were then deposited on all the three spray coated SiO_2/Si substrates by e-beam evaporation techniques covering with aluminium masks as depicted in Fig. 3.11. ~100 nm thick Au was deposited as the electrode materials. The detailed steps behind the sensor fabrication are depicted in chapter 3.

5.3.4 VOC sensing

To judge the natural selectivity, all the three sensors (S_1-S_3) were exposed to the different groups of organic vapours like alcohols, aldehyde, ketone, aromatic hydrocarbons etc. Detection limit and operating temperature was 100 ppm and 150°C, respectively. All the three sensors (S_1-S_3) exhibited highest sensitivity towards formaldehyde where pure C_{60} (S_1), TiO_2

nanoparticles (S_2) and C_{60}-TiO_2 hybrid (S_3) showed 40%, 48% and 117% response towards 100 ppm of formaldehyde at 150°C (Fig. 5.17(a)). Based on the overall selectivity performance of all the sensors, formaldehyde was considered as the target VOC to study the temperature effect, transient behaviour, response/recovery characteristics etc.
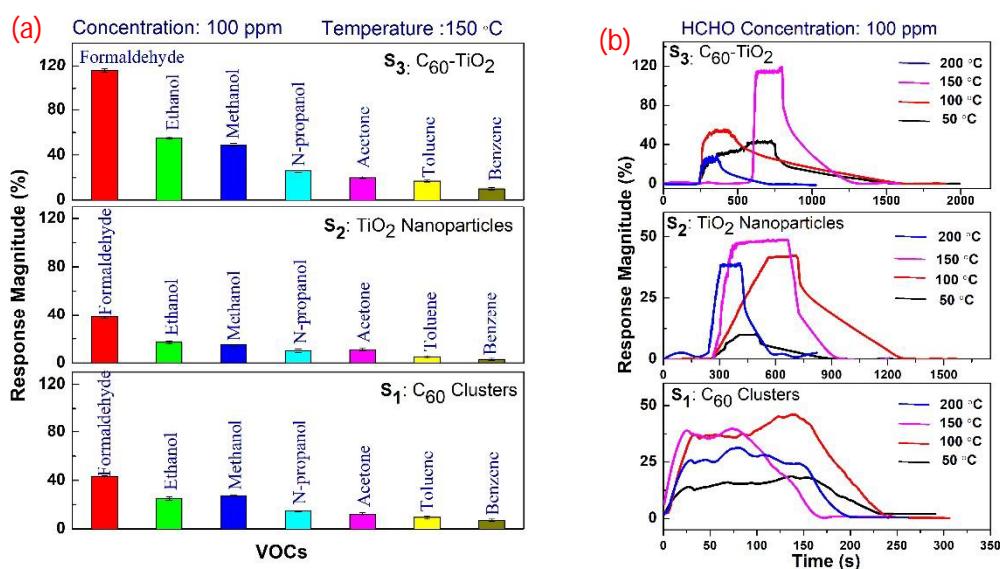
Fig. 5.17. (a) Natural selectivity tested for S_1-S_3 sensors in exposure to 100 ppm of different VOCs at 150 °C, (b) response characteristics of all the three sensors at variable operating temperature (50 °C to 200 °C) in the exposure of 100 ppm of formaldehyde.

All the sensors were tested at four different temperatures i.e. 50 °C, 100 °C, 150 °C and 200 °C in 100 ppm of formaldehyde (Fig. 5.17 (b)). S_1 exhibited highest and almost equal response magnitude at 100 °C and 150 °C. Response was decreased at both the very low (50 °C) and very high (200 °C) temperature as shown in Fig. 5.17(b). S_2 also showed highest response magnitude at 150 °C (49%) and appreciably good response magnitude at 100 °C (34%) and 200 °C (41%). C_{60} encapsulated TiO_2 NPs sensor (S_3) exhibited overall higher response magnitude as compared to other two sensors (Fig. 5.17 (b)). At 150°C, S_3 showed noticeably very high response magnitude of 117% in 100 ppm formaldehyde. But the response was comparatively low at both the 100 °C and 200 °C for S_3. Therefore, 150 °C was treated as the optimized temperature in the current sensor study.

Transient response of all the three sensors (S_1-S_3) were examined towards formaldehyde within the concentration range of 1 ppm to 1000 ppm at 150 °C as shown in Fig. 5.17 (a). Resistance was increased in case of S_2 and S_3 whereas decreased in case of S_1 in the exposure to the reducing vapor formaldehyde (Fig. 5.17(a)).
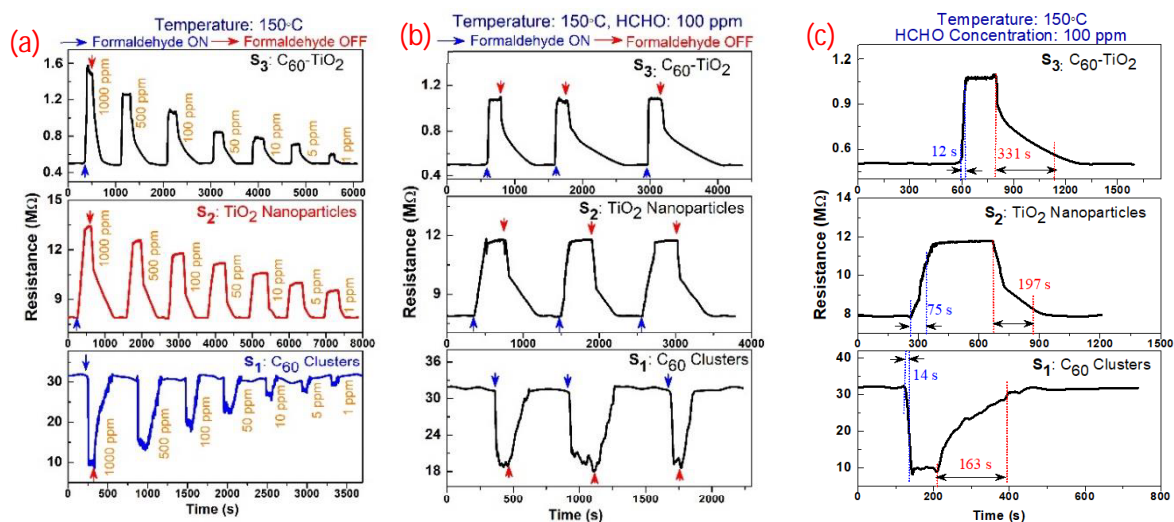
Fig. 5.18. (a) Transient behaviour within the formaldehyde concentration range of 1 to 1000 ppm, (b) repeated cycle characteristics, and (c) response/recovery characteristics measured at 150°C.

TiO$_2$ nanoparticles (S$_2$) exhibited stable *p*-type conductivity as the Ti-vacancy was dominated over the oxygen vacancy as discussed in chapter 2 and 3. On exposure to formaldehyde, electrons are released to the TiO$_2$ nanoparticle where some of the hole undergoes recombination and thereby resistance is increased. On the other hand, C$_{60}$ (S$_1$) which is known as electron rich materials [43], exhibited n-type conductivity and decreased value of resistances in the exposure of formaldehyde (Fig. 5.18 (a)). However, the C$_{60}$ encapsulated TiO$_2$ NPs (S$_3$) showed *p*-type conductivity as dominated by the behaviour of TiO$_2$ nanoparticles.

While, S$_2$ and S$_3$ showed very stable base line resistances, S$_1$ exhibited a slightly noisy baseline at 150 °C clearly evidenced in Fig. 5.18(a) and (b). The noisy nature of the S$_1$ sensors is also visible in the transient response and repeated cycle behaviour in Fig. 5.18(a) and (b), respectively.

Pure C$_{60}$ i.e. S$_1$ exhibited short response time (14 s) and recovery time (163 s). On the other hand, pure TiO$_2$ nanoparticles (S$_2$) took comparatively long response time (75 s) and recovery time (197 s). C$_{60}$-TiO$_2$ NPs hybrid exhibited shortest response time (12 s) but a long recovery time (331 s) among all the sensors (S$_1$ and S$_2$). The response/recovery time measurement for all the sensors is represented in Fig. 5.18(c).

Fig. 5.19 represents the comparative response magnitude of all the sensors for a total concentration range of 1 to 1000 ppm. With synergistic effects of both TiO$_2$ nanoparticles and C$_{60}$ clusters, the C$_{60}$ encapsulated TiO$_2$ NPs hybrid showed a highest response magnitude throughout the concentration range (1 to 1000 ppm) of formaldehyde. The detection in 1 ppm

with a fair response magnitude of 22 % was achieved with C_{60}-TiO_2 (S_3) sensor. More than two times increase in the response magnitude was recorded in C_{60}-TiO_2 (S_3) sensor (117%) in comparison with pure S_2 (48%) and S_1 (41%) towards 100 ppm of formaldehyde at 150°C (Fig. 5.19).
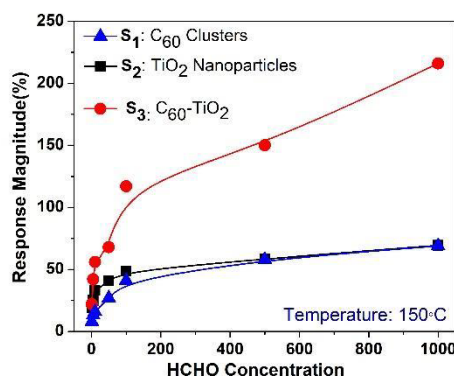
Fig. 5.**19** Response magnitude as a function of formaldehyde concentrations.

5.3.5 Sensing mechanism
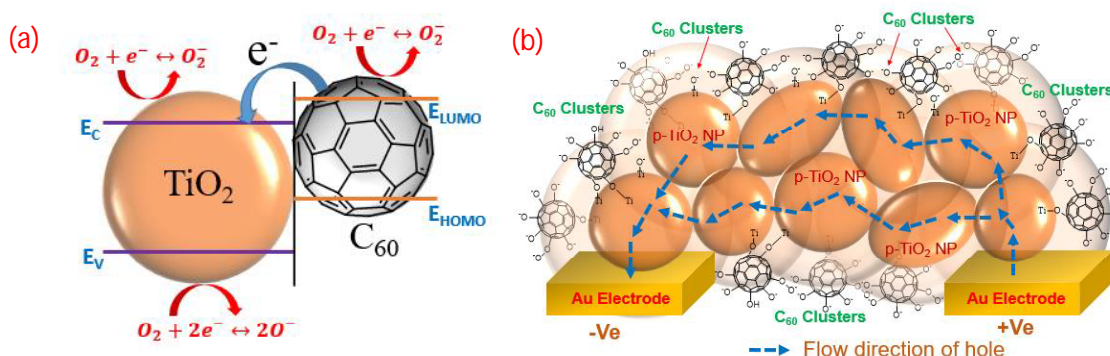
Fig. 5.20. (a) Energy level diagram of C_{60}-TiO_2 composite indicating possible flow of electron in air ambient, (b) Schematic view of the C_{60} encapsulated TiO_2 nanoparticles layer in-between two electrodes.

C_{60} depicting *n*-type conductivity is highly influenced by adsorbed surface oxygen groups which acts as an outstanding electron acceptor [60]. In the current study, hydrated fullerene, having abundant adsorbed oxygen groups (hydroxyl and epoxy) were formed in the first stage. Then the hydrated fullerene formed covalent bonds with TiO_2 nanoparticles and developed C_{60} encapsulated TiO_2 nanoparticle hybrid. On the formation of hybrid, the existence of Ti-O-C linkage is confirmed with X-ray photo spectroscopy in Fig. 5.16(b) and (c). Further thermal annealing at high temperature, enhanced the number of reactive oxygen species (O_2^-, O^- and O^{2-}) and reduced the number of hydroxyl and epoxy to the functionalized C_{60} surface. Oxidized C_{60}

being more reactive in nature possesses more interaction sites and thus provides a fair response magnitude with very short response time [60].

Electron affinity of anatase TiO_2 (~5.1 eV) [43] is quite high rather than the electron affinity of fullerene and electron can transfer from lowest unoccupied molecular orbital (LUMO) to the conduction band of the TiO_2 [42]. Excess electrons, injected to the TiO_2 then take part in formation of O_2^- from O_2 in air ambient [43]. Similar reaction can also occur at the surface of the C_{60} as shown in Fig. 5.20(a). C_{60} enhances movement of electrons in-between TiO_2 and C_{60} possibly due to the triply degenerate low lying lowest unoccupied molecular orbital (LUMO) and the delocalized π structure of C_{60} [16],[61]. On the other hand, TiO_2 nanoparticles owing to the Ti vacancy dominated nature, exhibit stable p-type conductivity. The Ti vacancy donated holes become effective over the free electron provided by the oxygen vacancy type defects [58]. Therefore, in air ambient, functionalized oxygen species effectively reduce the electron concentration in p-TiO_2 nanoparticles as well as in C_{60} that eventually increase electron deficiency both in the C_{60} and p-TiO_2 nanoparticles. Therefore, a hole accumulation takes place near the p-TiO_2 surface increasing the overall conductivity of the composite.
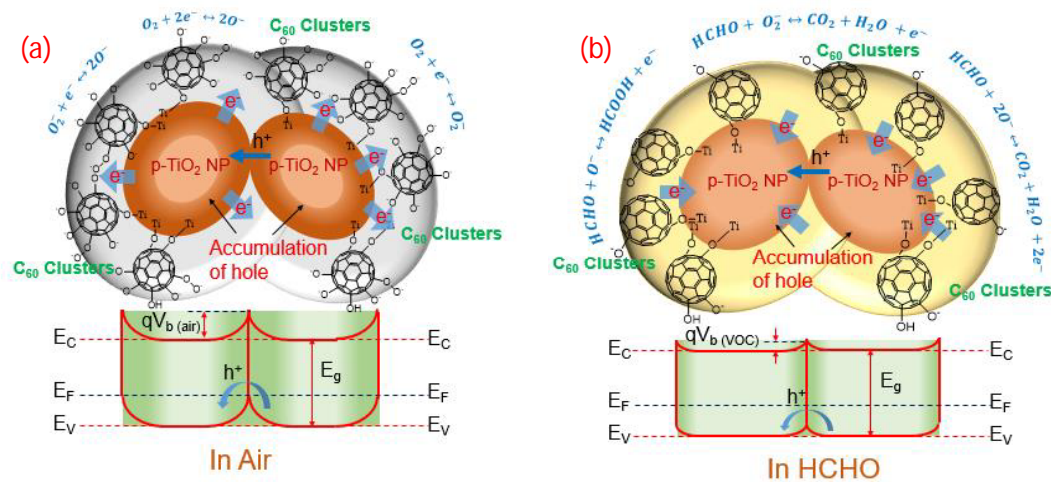
Fig. 5.21 Sensing mechanism in C_{60} encapsulated TiO_2 nanoparticles with the help of energy band diagram in (a) air and, (b) formaldehyde.

Sensor results in Fig. 5.18(a) distinctly shows two important factors i.e. (i) p-type conductivity in C_{60}-TiO_2 composite where individually C_{60} exhibits n-type and TiO_2 nanoparticles shows p-type conductivity and (ii) baseline resistance in C_{60}-TiO_2 composite (0.5 MΩ) decreased significantly as compared to the pure C_{60} (31 MΩ) and TiO_2 nanoparticles (8 MΩ). So, these two observations confirms that (i) the current transport in C_{60}-TiO_2 composite (S_3) is occurred mostly through the TiO_2 nanoparticles and (ii) the holes are accumulated to the p-TiO_2 nanoparticle interface lowering the effective resistance of the C_{60}-TiO_2 composite sensor (S_3).

However, considering the above two facts, a schematic of the C_{60} encapsulated TiO_2 nanoparticles layer in-between two electrodes is represented in Fig. 5.20 (b) indicating the direction of the flow of holes inside the channel under biasing condition.

Now, the C_{60}-TiO_2 composite is considered separately in air and in the exposure of formaldehyde. In air ambient, oxygen functionalized C_{60} behaves like an electron acceptor and extracted electron from p-TiO_2 creating hole accumulation near the TiO_2 NPs interface as shown in the Fig. 5.21(a). The energy band diagram in Fig. 5.21(a) shows the corresponding band bending and the created built-in-potential ($qV_{b(air)}$) near the surface in air ambient. Fig. 5.21(b) shows the removal of surface oxygen in C_{60} due to the reactions with HCHO that eventually donate electrons back to the TiO_2 nanoparticles lowering the band bending as well as the built-in-potential ($qV_{b(VOC)}$) near the surface. If, I_0 is the current in flat band condition (i.e. no built-in-potential), current in air and VOC ambient can be written as in Eq.5.4.

$$I_{air/VOC} = I_0 exp\left[\frac{qV_{b(air)/(VOC)}}{kT}\right] \tag{5.4}$$

Where, k is the Boltzmann's constant and T is the temperature [62]. Now, the response of the sensor (S_G) can be written as in Eq.5.5.

$$S_G \approx exp\left[\frac{q\left(V_{b(air)} - V_{b(VOC)}\right)}{kT}\right] \times 100 \tag{5.5}$$

Moreover, high response magnitude of the C_{60}-TiO_2 composite can be attributed due to the inbuilt porous and spongy structure of fullerene that provides enormous reaction sites for the reducing vapours [17],[23]. On the other hand, easy exchange of electrons between C_{60} and TiO_2 influences the hole current significantly, exhibiting very high ambient sensitivity by the C_{60} encapsulated TiO_2 nanoparticles sensor.

5.4 Conclusions

In the current chapter, highly sensitive sensors were developed by establishing C_{60}-TiO_2 nanostructures based composite for the detection of VOCs till ppb level. Ultra-high response magnitude towards formaldehyde was obtained with fast response and recovery time for the nanocomposite sensors. All the C_{60}-TiO_2 nanostructures were examined through different characterization techniques. All the C_{60}-TiO_2 nanostructures sensors showed their natural selectivity towards formaldehyde as compared to other tested VOCs. Therefore, sensor study was carried out by considering formaldehyde as the target species. 150 ℃ was found as the

optimized temperature where all the nanocomposite sensors showed excellent response magnitude (>92%) to 100 ppm of formaldehyde.

Eminently oriented one dimensional TiO_2 nanotubes were synthesized via electrochemical anodization route which were then decorated with zero dimensional, functionalized fullerene-C_{60} through hydrothermal route. Four C_{60}-TiO_2 nanotube composites (S_1-S_4) with varied concentration of fullerene (0.006 wt%, 0.01 wt%, 0.02 wt% and 0.05 wt%) were synthesized and characterized. S_4 having 0.05 wt% of fullerene showed the highest response of 99.6% towards 100 ppm formaldehyde at 150°C where as S_3 having 0.02 wt % of fullerene showed fastest response/recovery of 4 s/ 7 s among all the sensors at the same conditions. Being an ultra-high sensitivity towards formaldehyde, the lower detection limit was extended up to 100 ppb.

Extraordinary high formaldehyde sensing was observed in the in the C_{60}- TiO_2 nanoparticle composite sensors within the broad concentration range of 1 ppm to 1000 ppm at 150 °C. As compared to the pure form of C_{60} and TiO_2, composite showed more than double response magnitude (117 % in 100 ppm formaldehyde at 150 °C) with appreciably fast response time (12 s).

References

1. S. Sutradhar, A. Patnaik, A new fullerene-C_{60}–Nanogold composite for non-enzymatic glucose sensing, Sensors and Actuators B: Chemical 241 (2017) 681-689.

2. X. Wang, F. Tang, X. Qi, Z. Lin, D. Battocchi, X. Chen, Enhanced Protective Coatings Based on Nanoparticle fullerene C_{60} for Oil & Gas Pipeline Corrosion Mitigation, Nanomaterials 9 10 (2019) 1476.

3. X. Fan, N. Soin, H. Li, H. Li, X. Xia, J. Geng, Fullerene (C_{60}) nanowires: the preparation, characterization, and potential applications, Energy & Environmental Materials (2020).

4. S. Afreen, K. Muthoosamy, S. Manickam, U. Hashim, Functionalized fullerene (C_{60}) as a potential nanomediator in the fabrication of highly sensitive biosensors, Biosensors and Bioelectronics 63 (2015) 354-364.

5. J. Wu, L. B. Alemany, W. Li, L. Petrie, C. Welker, J. D. Fortner, Reduction of hydroxylated fullerene (fullerol) in water by zinc: reaction and hemiketal product characterization, Environmental science & technology 48 13 (2014) 7384-7392.

6. G.V Andrievsky, M. V. Kosevich, M. Vovk, V. S. Shelkovsky, L. A. Vashchenko, On the production of an aqueous colloidal solution of fullerenes, Journal of the Chemical Society, Chemical Communications 12 (1995) 1281-1282.

7. X. Wei, M. Wu, L. Qi, Z. Xu, Selective solution-phase generation and oxidation reaction of C_{60} n-(n= 1, 2) and formation of an aqueous colloidal solution of C_{60}, Journal of the Chemical Society, Perkin Transactions *2* 7 (1997) 1389-1394.

8. J.A. Brant, J. Labille, J. Y. Bottero, M. R. Wiesner, Characterizing the impact of preparation method on fullerene cluster structure and chemistry, Langmuir 22 8 (2006) 3878-3885.

9. S. Bosi, T. D. Ros, G. Spalluto, Maurizio Prato, Fullerene derivatives: an attractive tool for biological applications, European journal of medicinal chemistry 38 11-12 (2003) 913-923.

10. X. Ou, X. Tan, S. Wei, S. Chen, J. Zhang, X. Liu, Electrochemiluminescence biosensor for cholesterol detection based on AuNPs/l-cys–C_{6}0 nanocomposites, Analytical Methods 6 11 (2014) 3804-3810.

11. D.A. Britz, A.N. Khlobystov, J. Wang, A. S. O'Neil, M. Poliakoff, A. Ardavan, G. A. D. Briggs, Selective host–guest interaction of single-walled carbon nanotubes with functionalised fullerenes, Chemical communications 2 (2004) 176-177.

12. Y.I. Prylutskyy, V. I. Petrenko, O. I. Ivankov, O. A. Kyzyma, L. A. Bulavin, O. O. Litsis, M. P. Evstigneev, V. V. Cherepanov, A. G. Naumovets, U. Ritter, On the origin of C_{60} fullerene solubility in aqueous solution, Langmuir 30 14 (2014) 3967-3970.

13. D. Long, M. Li, H. Wang, H. Wang, Y. Chai, R. Yuan, A photoelectrochemical biosensor based on fullerene with methylene blue as a sensitizer for ultrasensitive DNA detection, Biosensors and Bioelectronics 142 (2019) 111579.

14. N. Furuuchi, R. G. Shrestha, Y. Yamashita, T. Hirao, K. Ariga, L. K. Shrestha, Self-Assembled Fullerene Crystals as Excellent Aromatic Vapor Sensors, Sensors 19 2 (2019) 267.

15. J.A. Rather, K.D. Wael, Fullerene-C_{60} sensor for ultra-high sensitive detection of bisphenol-A and its treatment by green technology, Sensors and Actuators B: Chemical 176 (2013) 110-117.

16. D. Smazna, J. Rodrigues, S. Shree, V. Postica, G. Neubüser, A. F. Martins, N. B. Sedrine, N.K. Jena, L. Siebert, F. Schutt, O. Lupan, R. Ahuja, M.R. Correia, T. Monterio, L. Kienle, Y. Yang, R. Adelung, Y.K. Mishra, Buckminsterfullerene

hybridized zinc oxide tetrapods: defects and charge transfer induced optical and electrical response, Nanoscale 10 21 (2018) 10050-10062.

17. S. Keshtkar, A. Rashidi, M. Kooti, M. Askarieh, S. Pourhashem, E. Ghasemy, Nosrat Izadi, A novel highly sensitive and selective H2S gas sensor at low temperatures based on SnO$_2$ quantum dots-C$_{60}$ nanohybrid: experimental and theory study, Talanta 188 (2018) 531-539.

18. Z. Wang, T. Hu, R. Liang, M. Wei Application of Zero-Dimensional Nanomaterials in Biosensing, Frontiers in Chemistry 8 (2020) 320.

19. M.A. Einarsrud, T. Grande, 1D oxide nanostructures from chemical solutions, Chemical Society Reviews 43 7 (2014) 2187-2199.

20. A. Hazra, K. Dutta, B. Bhowmik, P. P. Chattopadhyay, P. Bhattacharyya, Room temperature alcohol sensing by oxygen vacancy controlled TiO$_2$ nanotube array, Applied Physics Letters 105 8 (2014) 081604.

21. G.V. Andrievsky, V. K. Klochkov, A. B. Bordyuh, G. I. Dovbeshko, Comparative analysis of two aqueous-colloidal solutions of C$_{60}$ fullerene with help of FTIR reflectance and UV–Vis spectroscopy, Chemical Physics Letters 364 1-2 (2002) 8-17.

22. Y. Park, N. J. Singh, K. S. Kim, T. Tachikawa, T. Majima, Wonyong Choi, Fullerol–titania charge-transfer-mediated photocatalysis working under visible light, Chemistry–A European Journal 15 41 (2009) 10843-10850.

23. M.M. Ali, K. Y. Sandhya, Visible light responsive titanium dioxide–cyclodextrin–fullerene composite with reduced charge recombination and enhanced photocatalytic activity, Carbon 70 (2014): 249-257.

24. J. Yu, T. Ma, G. Liu, B. Cheng, Enhanced photocatalytic activity of bimodal mesoporous titania powders by C$_{60}$ modification, Dalton Transactions 40 25 (2011) 6635-6644.

25. S. Henke, K. H. Thürer, J. K. N. Lindner, B. Rauschenbach, B. Stritzker, Structural characterization of the temperature dependence of C$_{60}$-thin films on mica (001) by x-ray diffraction, Journal of applied physics 76 6 (1994) 3337-3340.

26. K.L Akers, C. Douketis, T. L. Haslett, M. Moskovits, Raman spectroscopy of C$_{60}$ solid films: a tale of two spectra, The Journal of Physical Chemistry 98 42 (1994) 10824-10831.

27. J. Lin, R. Zong, M. Zhou, Y, Zhu, Photoelectric catalytic degradation of methylene blue by C60-modified TiO$_2$ nanotube array, Applied Catalysis B: Environmental 89 3-4 (2009) 425-431.

28. Y. Zhang, Y. Du, J. R. Shapley, M. J. Weaver, Surface-enhanced Raman spectroscopy of electroactive films of C_{60} and an Ir-C_{60} complex on gold: symmetry lowering, electron localization, and countercation effects, Chemical physics letters 205 6 (1993) 508-514.

29. R. K. Mani, S. Ganesan, P. Aruna, Synthesis and optical limiting studies of Au-doped TiO_2 nanoparticles, Advances in Natural Sciences: Nanoscience and Nanotechnology 2 (2011) 025012.

30. S. Wang, C. K. Dai, P. Cai, H. Chen, C. Yang, Q. Huang, Fullerene C_{70}–TiO_2 hybrids with enhanced photocatalytic activity under visible light irradiation Journal of Materials Chemistry A 3, no. 42 (2015) 21090-21098.

31. A. Hazra, B. Bhowmik, K. Dutta, P. P. Chattopadhyay, P. Bhattacharyya, Stoichiometry, length, and wall thickness optimization of TiO_2 nanotube array for efficient alcohol sensing, ACS applied materials & interfaces, 7 18 (2015) 9336-9348.

32. Q. Cai, Z. Hu, Q. Zhang, B. Li, Z. Shen, Fullerene (C_{60})/CdS nanocomposite with enhanced photocatalytic activity and stability, Applied Surface Science 403 (2017) 151-158.

33. P. Bindra, S. Gangopadhyay, Arnab Hazra, Au/TiO_2 Nanotubes/Ti-based solid-state vapor sensor: Efficient sensing in resistive and capacitive modes, IEEE Transactions on Electron Devices 65 5 (2018) 1918-1924.

34. A. Hazra, P. Bhattacharyya, Tailoring of the gas sensing performance of TiO_2 nanotubes by 1-D vertical electron transport technique, IEEE Transactions on Electron Devices 61 10 (2014) 3483-3489.

35. W. Li, S. Ma, Y. Li, G. Yang, Y. Mao, J. Luo, D. Gengzang, X. Xu, S. Yan, Enhanced ethanol sensing performance of hollow ZnO–SnO_2 core–shell nanofibers, Sensors and Actuators B: Chemical 211 (2015): 392-402

36. L. Liu, S. Li, J. Zhuang, L. Wang, J. Zhang, H. Li, Z. Liu, Y. Han, X. Jiang, P. Zhang, Improved selective acetone sensing properties of Co-doped ZnO nanofibers by electrospinning, Sensors and actuators B: chemical 155, no. 2 (2011): 782-788.

37. Q. Chen, S. Y. Ma, X. L. Xu, H. Y. Jiao, G. H. Zhang, L. W. Liu, P. Y. Wang, D. J. Gengzang, H. H. Yao. Optimization ethanol detection performance manifested by gas sensor based on In_2O_3/ZnS rough microspheres. Sensors and Actuators B: Chemical 264 (2018): 263-278.

38. A.K Sharma, A. Mahajan, R. K. Bedi, S. Kumar, A. K. Debnath, and D. K. Aswal, CNTs based improved chlorine sensor from non-covalently anchored multi-walled carbon nanotubes with hexa-decafluorinated cobalt phthalocyanines, RSC advances 7 78 (2017) 49675-49683.

39. S. Liu, B. Yu, H. Zhang, T. Fei, T. Zhang, Enhancing NO_2 gas sensing performances at room temperature based on reduced graphene oxide-ZnO nanoparticles hybrids, Sensors and actuators B: chemical 202 (2014) 272-278.

40. G. Korotcenkov, I. Blinov, V. Brinzari, J. R. Stetter, Effect of air humidity on gas response of SnO2 thin film ozone sensors. Sensors and Actuators B: Chemical 122, (2007): 519-526.

41. R. Ionescu, A. Vancu, C. Moise, and A. Tomescu, Role of water vapour in the interaction of SnO_2 gas sensors with CO and CH_4, Sensors and Actuators B: Chemical 61, (1999): 39-42.

42. H. Liang, S. Xu, W. Liu, Y. Sun, X. Liu, X. Zheng, S. Li et al. Modulation of the work function of fullerenes C_{60} and C_{70} by alkali-metal adsorption: A theoretical study, Physics Letters A 377 (2013): 2676-2680.

43. D. O. Scanlon, C.W. Dunnill, J. Buckeridge, S. A. Shevlin, A. J. Logsdail, S. M. Woodley, C. R. A. Catlow, M. J. Powell, R. G. Palgrave, I. P. Parkin, G. W. Watson, T. W. Keal, P. Sherwood, A. Walsh, A. A. Sokol Band alignment of rutile and anatase TiO_2, Nature materials 12 (2013) 798.

44. A. Hazra, P. Bhattacharyya, Role of junction geometry in determining the rectification performance of nanostructured TiO_2-based pn junctions, IEEE Transactions on Electron Devices 62 (2015) 1984-1990.

45. A. Hazra, S. K. Hazra, E. Bontempi, V. N. Lakshmi, S. Sinha, C. K. Sarkar, S. Basu. Anodically grown nanocrystalline titania thin film for hydrogen gas sensors—a comparative study of planar and MAIM device configurations, Sensors and Actuators B: Chemical 188 (2013) 787-796.

46. G. Sberveglieri, G. Faglia, C. Perego, P. Nelli, R. N. Marks, T. Virgili, C. Taliani, and R. Zamboni, Hydrogen and humidity sensing properties of C_{60} thin films, Synthetic metals 77 1-3 (1996) 273-275.

47. P. Schulz, L. L. Kelly, P. Winget, H. Li, H. Kim, P. F. Ndione, A. K. Sigdel, J.J. Berry, S.Graham, J.M. Bredas, A. Kahn, O.L.A Monti, Tailoring Electron-Transfer Barriers for Zinc Oxide/C_{60} Fullerene Interfaces, Advanced Functional Materials 24 46 (2014) 7381-7389.

48. L. Nie, J. Yu, M. Jaroniec, F.F. Tao, Room-temperature catalytic oxidation of formaldehyde on catalysts, Catalysis Science Technology 6 (2016) 3649

49. Y. K. Jo, S-Y. Jeong, Y. K. Moon, Y-M. Jo, J-W. Yoon, J-H. Lee, Exclusive and ultrasensitive detection of formaldehyde at room temperature using a flexible and monolithic chemiresistive sensor, Nature Communication 12 (2021) 4955 (1-9)

50. P. Kowalczyk, J. Miyawaki, Y. Azuma, S-H. Yoon, K. Nakabayashi, P.A. Gauden, S. Furmaniak, A.P. Terzyk, M. Wisniewski, J. Włoch, K. Kaneko, A.V. Neimark, Molecular simulation aided nanoporous carbon design for highly efficient low-concentrated formaldehyde capture, Carbon 124 (2017) 152-160

51. H. Rong, Z. Ryu, J. Zheng, Y. Zhang, Influence of heat treatment of rayon-based activated carbon fibers on the adsorption of formaldehyde, Journal of Colloid and Interface Science 261 (2003) 207–212

52. Y. Song, W. Qiao, S-H. Yoon, I. Mochida, Q. Guo, L. Liu, Removal of formaldehyde at low concentration using various activated carbon fibers, Journal of Applied Polymer Science 106 (2007) 2151–2157

53. K. J. Lee, N. Shiratori, G.H. Lee, J. Miyawaki, I. Mochida, S-H. Yoon, J. Jang, Activated carbon nanofiber produced from electrospun polyacrylonitrile nanofiber as a highly efficient formaldehyde adsorbent, Carbon 48 (2010) 4248 –4255

54. C.L. Mangun, K.R. Benak, M.A. Daley, J. Economy, Oxidation of activated carbon fibers: effect on pore size, surface chemistry, and adsorption properties, Chemistry of Materials 11 (1999) 3476-3483.

55. A. Graja, I. Olejniczak, A. Bogucki, D. Bonifazi, F. Diederich, Chromophoric interaction in [60] fullerene – porphyrin dyads investigated by solid state UV-vis and IR spectroscopies, Chemical physics 300 (2004) 227-232.

56. J. Lin, R. Zong, M. Zhou, Y. Zhu, Photoelectric catalytic degradation of methylene blue by C_{60} modified TiO_2 nanotube array, Applied Catalysis B: Environmental 89 (2009) 425-431.

57. Y. Kanzawa, S. Hayashi, K. Yamamoto, Raman spectroscopy of Si rich films: possibility of Si cluster formation, Journal of Physics: Condensed Matter 8 26 (1996) 4823.

58. A. Hazra, S. Das, J. Kanungo, C. K. Sarkar, S. Basu, Studies on resistive gas sensor based on sol-gel grown nanocrystalline p-TiO_2 thin film for fast hydrogen detection, Sensors and Actuators B: Chemical 183 (2013) 87-95.

59. G. Sberveglieri, G. Faglia, C. Perego, P. Nelli, R. N. Marks, T. Virgili, C. Taliani, R. Zamboni, Hydrogen and humidity sensing properties of C_{60} thin films, Synthetic metals 77 (1996) 273-275.

60. A. P. Saab, M. Laub, V. I. Srdanov, G. D. Stucky, Oxidized thin films of C_{60}: A new humidity sensing material, Advanced Materials 10 6 (1998) 462-465.

61. R. Koeppe, N. S. Sariciftci, Photoinduced charge and energy transfer involving fullerene derivatives, Photochemical & Photobiological Sciences 5 12 (2006) 1122-1131.

62. A. Teleki, E. Sotiris, P. K. Kalyanasundaram, P. I. Gouma, Sensing of organic vapours by flame-made TiO_2 nanoparticles, Sensors and actuators B: chemical 119 2 (2006) 683-690.